SANDIA REPORT
SAND2020-10360
Printed September 2020

Sandia National Laboratories

A Quantum Analog Coprocessor for Correlated Electron Systems Simulation

Andrew D. Baczewski, Mitchell I. Brickson, Quinn Campbell, N. Tobias Jacobson, and Leon N. Maurer

Prepared by
Sandia National Laboratories
Albuquerque, New Mexico 87185
Livermore, California 94550

Issued by Sandia National Laboratories, operated for the United States Department of Energy by National Technology & Engineering Solutions of Sandia, LLC.

Available to DOE and DOE contractors from

U.S. Department of Energy
Office of Scientific and Technical Information
P.O. Box 62
Oak Ridge, TN 37831

Telephone: (865) 576-8401
Facsimile: (865) 576-5728
E-Mail: reports@osti.gov
Online ordering: http://www.osti.gov/scitech

Available to the public from

U.S. Department of Commerce
National Technical Information Service
5301 Shawnee Road
Alexandria, VA 22312

Telephone: (800) 553-6847
Facsimile: (703) 605-6900
E-Mail: orders@ntis.gov
Online order: https://classic.ntis.gov/help/order-methods

ABSTRACT

Analog quantum simulation is an approach for studying physical systems that might otherwise be computationally intractable to simulate on classical high-performance computing (HPC) systems. The key idea behind analog quantum simulation is the realization of a physical system with a low-energy effective Hamiltonian that is the same as the low-energy effective Hamiltonian of some target system to be studied. Purpose-built nanoelectronic devices are a natural candidate for implementing the analog quantum simulation of strongly correlated materials that are otherwise challenging to study using classical HPC systems. However, realizing devices that are sufficiently large to study the properties of a non-trivial material system (e.g., those described by a Fermi-Hubbard model) will eventually require the fabrication, control, and measurement of *at least* $O(10)$ quantum dots, or other engineered quantum impurities. As a step toward large-scale analog or digital quantum simulation platforms based on nanoelectronic devices, we propose a new approach to analog quantum simulation that makes use of the large Hilbert space dimension of the electronic baths that are used to adjust the occupancy of one or a few engineered quantum impurities.

This approach to analog quantum simulation allows us to study a wide array of quantum impurity models. We can further augment the computational power of such an approach by combining it with a classical computer to facilitate dynamical mean-field theory (DMFT) calculations. DMFT replaces the solution of a lattice impurity problem with the solution of a family of localized impurity problems with bath couplings that are adjusted to satisfy a self-consistency condition between the two models. In DMFT, the computationally challenging task is the high-accuracy solution of an instance of a quantum impurity model that is determined self-consistently in coordination with a mean-field calculation. We propose using one or a few engineered quantum impurities with adjustable couplings to baths to realize an analog quantum coprocessor that effects the solution of such a model through measurements of a physical quantum impurity, operating in coordination with a classical computer to achieve a self-consistent solution to a DMFT calculation.

We focus on implementation details relevant to a number of technologies for which Sandia has design, fabrication, and measurement expertise. The primary technical advances outlined in this report concern the development of a supporting modeling capability. As with all analog quantum simulation platforms, the successful design and operation of individual devices depends critically on one's ability to predict the effective low-energy Hamiltonian governing its dynamics. Our project has made this possible and lays the foundation for future experimental implementations.

ACKNOWLEDGEMENTS

We are grateful for countless hours of useful conversations with our colleagues, many of which preceded this project.

- Experimental insights and grounding
  - Malcolm Carroll
  - Ryan Jock
  - Tzu-Ming Lu
  - Dwight Luhman
  - Shashank Misra
  - Peter Sharma
  - Lisa Tracy
  - Dan Ward
- Theoretical sympathizers
  - Robin Blume-Kohout
  - Ray Clay
  - John King Gamble
  - Jonathan Moussa
  - Rick Muller
  - Mohan Sarovar
  - Luke Shulenburger
  - Wayne Witzel
- General wisdom
  - John Aidun

We are also grateful to our collaborators at the University of New South Wales. In particular, we acknowledge many fruitful interactions with Serwan Asaad, Benni Joecker, Mark Johnson, Prof. Andrea Morello, and Vincent Mourik. Some of the theoretical effort in support of their demonstration of nuclear electric resonance was covered by this LDRD.

CONTENTS

LIST OF FIGURES

TERMS AND DEFINITIONS

Abbreviation	Definition
APAM	Atomic-precision advanced manufacturing
CAD	Computer-aided design
DMFT	Dynamical mean-field theory
EQI	Engineered quantum impurity
HPC	High-performance computing
MOS	Metal oxide semiconductor
NISQ	Noisy intermediate-scale quantum

1. INTRODUCTION

We begin by describing analog quantum simulation in Section 1.1, contrasting it with digital quantum simulation in particular. We then propose to use engineered quantum impurities (EQIs) in semiconductors as an analog quantum simulation platform for quantum impurity models in Section 1.2. We augment the power of such an approach by proposing an analog quantum coprocessor for dynamical mean-field theory (DMFT) calculations in Section 1.3. Finally, we briefly highlight the outcomes of this project in Section 1.4.

1.1. What is analog quantum simulation?

Quantum technologies offer the promise of powerful new approaches to simulating physical systems. In the early 1980s, Richard Feynman was among the first to speculate about the possibility that a quantum computer is ultimately necessary to accurately simulate quantum mechanical systems [3]. Even going back to Dirac in 1929 [4], it has long been understood that the models governing generic quantum mechanical systems are "much too complicated" to be solved analytically, semi-analytically, or even numerically using increasingly capable classical computers in the intervening decades. One of the key distinguishing features of quantum mechanical systems is that the dimension of the state space (Hilbert space) that describes them grows exponentially in the number of degrees of freedom (e.g., electrons, atoms, quarks, qubits, etc.). Further, the principle of quantum superposition means that a valid state for such a system to exist in need not consist of amplitude on a single basis vector, but potentially exponentially many. Thus, in aggressively overly simplistic terms, the accurate simulation of an arbitrary quantum mechanical system on a computer requires a computer that can represent such superpositions in an exponentially large state space.

In the time since Feynman's original speculation, he has been shown to have been correct [5]. Digital quantum simulation algorithms for studying the properties of quantum mechanical systems have been developed [6–9] and in many instances they are likely to achieve an exponential advantage over classical computing resources in doing so. These algorithms rely on encoding the Hilbert space of the physical system to be simulated in the Hilbert space of a register of qubits in a quantum computer. A particular encoded state is prepared in this register, realizing a digital representation of the system being studied. An auxiliary register of qubits is then entangled with the register representing the physical system while some unitary evolution is implemented[1]. The auxiliary register is then manipulated and measured, from which a single bit of some observable of the encoded system (e.g., its total energy) is extracted [11, 12].

While this approach to simulation is conceptually straightforward, its implementation on an actual quantum computer is likely to remain an outstanding technical challenge for years to come. To realize a quantum computer with simulation capabilities beyond those of classical HPC

[1] It is worth noting that there are approaches that do no require the addition of auxiliary qubits, but these are limited in what can be extracted in a single execution of the algorithm [10].

systems, the number of qubits and their requisite fidelities[2] are orders of magnitude larger than what is available today. For example, recent projections indicate that error-corrected execution of a state-of-the-art digital quantum simulation algorithm for the Fermi-Hubbard model [13, 14] will require $\sim 10^5 - 10^6$ physical qubits with error rates of $10^{-4} - 10^{-3}$, respectively [15]. As it stands, the largest digital quantum simulations that have been executed consist of variational simulations of the Hartree-Fock approximation to the ground state of a few small molecules on at most 12 noisy physical qubits [16]. In spite of these seemingly modest numbers the development of a quantum hardware platform that can execute such a calculation represents critical progress toward the goal of fault-tolerant quantum simulation, even if it is likely to remain many years away.

We conjecture that the primary advantage that a machine capable of fault-tolerant digital quantum simulation will provide over classical HPC is in accuracy. In fact, methods for efficiently approximating the properties of quantum systems are ubiquitous in the physical and chemical sciences and even predate the widespread use of classical digital computing technology, e.g., the Thomas-Fermi [17, 18] and Hartree-Fock methods [19–21]. Modern computational chemical and materials science has produced a wide array of options for such approximate simulation, ranging from density functional [22] and coupled cluster theories [23] to quantum Monte Carlo [24]. Roughly, these methods offer a trade off between computational cost and accuracy. Many of these methods achieve *useful* levels of accuracy with classical HPC resources scaling as a polynomial in the size of the system being simulated. However, it is likely the case that the cost of realizing *arbitrary* levels of accuracy will always scale as an exponential in the system size. In achieving arbitrary accuracy in the simulation of physical systems, fault-tolerant digital quantum computers are likely to provide an exponential advantage [7, 25].

So, we begin this report by recognizing that digital quantum algorithms for quantum simulation are likely to achieve an important but subtle advantage over classical algorithms for quantum simulation. However, this advantage will likely only be realized in a future in which orders of magnitude more qubits are available with error rates in an integrated setting that are also orders of magnitude lower than the current state of the art (see, e.g., Ref. [26] for a contemporaneous assessment of the state-of-the-art in testbeds comprised of superconducting qubits). It is useful to then consider whether there are opportunities to leverage quantum technologies to execute *useful* simulation tasks in the intervening years, while also supporting development toward the long-term goal of a fault-tolerant quantum computer that achieves an exponential advantage in efficient and accurate simulation with digital quantum algorithms. Analog quantum simulation is one such opportunity.

Analog quantum simulation is predicated on the idea that well-characterized and highly controllable quantum systems can realize low-energy effective Hamiltonians that are the same as the low-energy effective Hamiltonians of other physical systems [27–30]. Here, the equivalence of *only* the low-energy effective theories is *essential*. Two physical systems with Hamiltonians that are equivalent across all energy scales are physically indistinguishable and there is little utility in trying to replicate one with the other, aside from assessing reproducibility (e.g., that

[2] High fidelities or, equivalently, low error rates are needed to execute circuits without error to ensure accurate outcomes. As the desired simulation circuits get deeper, corresponding to improved accuracy in the digital quantum simulation, the requisite error rates decrease.

multiple samples of a particular material system have statistically indistinguishable properties). By instead focusing on a particular subspace one can imagine two or more physical systems that are indistinguishable within that subspace but distinguishable outside of it. This suggests a powerful opportunity. Given a naturally occurring physical system with a particular low-energy effective theory, one can build an analog quantum simulator that realizes the *same* theory within an engineered physical system that may provide a number of advantages. One advantage might be realized if the this theory is difficult (perhaps intractable) to study using classical computing resources. Analog quantum simulation might then provide a context in which the particular theory of the target physical system can be *validated*. Another advantage might occur if variations in the parameters of the theory are resource intensive to realize in naturally occurring physical systems. One example of this is the Fermi-Hubbard model, for which realizing variations in the doping fraction and Hubbard U/t ratio requires years of effort in materials synthesis and characterization [31]. Thus another advantage might occur in realizing a reconfigurable analog quantum simulator for which the parameters of the low-energy effective theory can be varied at a dramatically reduced cost. Unlike digital quantum simulation, these advantages aren't easily quantified in terms of improvements in accuracy but rather in terms of an improved understanding of the phenomenology of the effective theory.

Whether such an approach to simulation can be realized on a timescale intermediate to digital quantum simulation will be determined by the underlying sensitivity to errors in the fabrication and operation of an analog quantum simulator. The resource requirements for digital quantum simulation are so great, in part due to a lack of intrinsic robustness in digital quantum simulation algorithms. However, analog quantum simulation is likely to be robust to errors to the same extent that the physical systems they are simulating are thermodynamically stable. The idea that low-energy effective theories have a certain insensitivity to errors has its roots in notions of critical phenomena and universality [32, 33]. These notions are restricted to a particular setting in which there are thermodynamically many microscopic degrees of freedom, such that one can talk about a fixed point under transformations across many length scales. Notions of insensitivity to errors for quantum simulators that aren't thermodynamically large might be related to sloppy low-energy effective theories [34] or low purity of the relevant observables [35].

Ultimately, the fundamental limits to how well an analog quantum simulation can be executed on a given quantum platform are limited by our ability to characterize, control, and measure it. Quality characterization is critical so that we know the low-energy effective Hamiltonian that is being implemented in our analog quantum simulator. Controllability is essential to being able to adjust the parameters of that low-energy effective Hamiltonian with precision. Finally, the ability to accurately measure the system is ultimately the key determining factor in the type, accuracy, and precision of information that can be extracted from such a platform. In all cases, we can see that it is essential to have a reliable device-level model of an analog quantum simulation platform to facilitate design and operation.

1.2. Engineered quantum impurities in semiconductors

This report introduces a new approach to analog quantum simulation using semiconductor quantum technologies. It is based on using EQIs in highly controllable nanoelectronic devices to

simulate quantum impurity models. Generally an EQI is comprised of a semiconductor heterostructure with nanoscale gates patterned onto the device (see Fig. 1-1a). Voltages applied to these gates can be used to accumulate or deplete free charge carriers (e.g., electrons or holes) in nanometer regions of the heterostructure. With these devices we can precisely manipulate and measure one or a few such particles, and control their coupling to one or more adjacent thermodynamically large bath(s). The particular technologies that we focus on are lithographic quantum dots based on both holes and electrons, as well dopant-based devices fabricated using atomic precision advanced manufacturing (APAM) [36]. Each of these technologies is potentially dual-purpose, as they might also eventually be used as qubits in implementing digital quantum simulation (see, e.g., Refs. [37–41] for contemporaneous state-of-the-art qubit experiments spanning these technologies). While there has been significant development dedicated to qubits in these platforms, fabricating and controlling *enough* EQI-based qubits with error rates necessary for large-scale digital quantum simulation remains a long-term goal. However, intermediate applications in analog quantum simulation might help to develop these technologies toward that end goal.

The low-energy effective theory governing the behavior of the particles in the EQI is ultimately one of the $O(10\text{ nm})$ atomic-orbital-like states that describe the charged degrees of freedom that are mostly strongly coupled to the electrostatic controls. We will describe these states using a theory of their envelope functions (e.g., effective mass theory). The energy scale on which these states are separated from the bulk band structure of the underlying host crystal is $O(10\text{ meV})$, and relative to a bulk bandgap of $O(1\text{ eV})$[3]. As the thermal energy scale at room temperature is ≈ 30 meV, at least a 300-fold reduction in the operating temperature of an EQI is required to suppress excitations out of the low-energy subspace and for the particles in the bath region to remain degenerate. Accordingly, the devices that we are proposing to use for analog quantum simulation must operate at dilution refrigerator temperatures of 1 K or below, with 100 mK temperatures being preferable to achieve higher fidelity in few-particle measurements.

The use of the term "EQI" instead of the more common "quantum dot" is motivated by two subtleties. The first is that the confining potential for one of the technologies (APAM-fabricated dopant-based devices) is due to a combination of the attractive potential of one or more dopant atoms and externally impressed voltages on nanoelectronic gates. Thus is it not strictly a lithographic quantum dot as most of the confining potential is due to the Coulomb field of dopant nuclei. The second (and more important) is to reflect the intended use of these devices. It is not just the the charged particles occupying the confining potential that we are concerned with leveraging for analog quantum simulation. We are also interested in using the charged particles occupying nearby thermodynamically large baths to which the impurities are controllably coupled. In fact, by *strongly* coupling an EQI with a relatively small Hilbert space dimension to a bath with a significantly larger Hilbert space dimension, we aim to realize a composite system with a much larger Hilbert space dimension than just the EQI alone. This gives us the prospect of realizing a device with a small number of individual components that still manages to simulate a much larger quantum system.

We illustrate an exemplary EQI energy-level diagram in Fig. 1-1b. The key features of an EQI are

[3] In other words, thermal leakage into delocalized states near the band edge from which they are bifurcated is a more severe concern than excitations across the host material's bandgap.

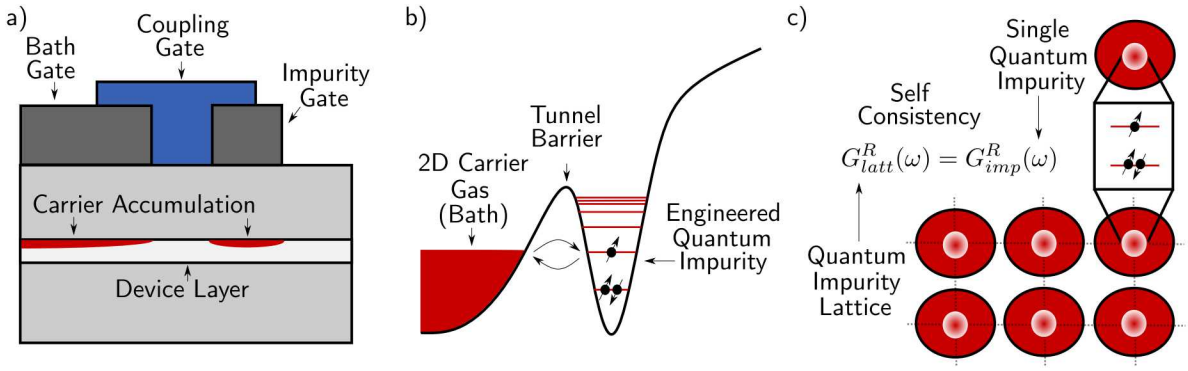

Figure 1-1 An exemplary EQI realizing an analog quantum simulation of a quantum impurity model and self-consistently adjusted to facilitate solution of a DMFT calculation. a) A cross-sectional view of a lithographic quantum dot in which bath and impurity gates are used to accumulate charge carriers at an interface in a semiconductor heterostructure. The coupling gate is used to tune the hybridization of the bath and impurity. b) An energy level diagram illustrating the coupling of the continuum of bath states to the discrete energy levels in the EQI through a tunnel barrier. The charge density in the bath, the bath-impurity hybridization, and the energy level structure of the EQI are all electrically tunable and a particular voltage configuration realizes an analog quantum simulation of a particular instance of a quantum impurity model (see Eqs. 1 and 2a-2c). c) The single impurity in our analog quantum simulator can be self-consistently adjusted to serve as a coprocessor for a DMFT calculation. In DMFT, the quantum impurity model parameters that realize a Green's function of a single quantum impurity are adjusted until they match the on-site Green's function for a lattice of quantum impurities.

the tunability of the bath, impurity, and their coupling. Specifically, we can adjust the density of the particles in the bath, the energy level structure of the impurity, and the energy-dependent coupling between the two. When EQIs are used as qubits, one typically reduces the coupling between the bath and impurity during coherent operation, and an appreciable tunnel coupling is only maintained during preparation and measurement. For analog quantum simulation of a quantum impurity model, we are interested in a regime in which the bath and impurity are strongly coupled while the impurity remains in a few-particle state on average. The motivation for this is to effect analog quantum simulation of a computationally challenging strongly correlated regime of the quantum impurity model. That such regimes are possible to achieve is motivated by the observation of the Kondo effect in lithographic quantum dots in GaAs [42–44], noting that this is more challenging in the material platforms that we are primarily concerned with. Later we will see that one of the key challenges for studying such strongly coupled systems is the representation of states that are strongly hybridized between the EQI and bath. One of the contributions of this project has been the implementation of new methods for studying these states, described in Section 3.2.

From Fig. 1-1b it is evident that a single EQI is a natural realization of a quantum impurity model. Later in the report (Section 2.1) we provide a mathematical statement of a generic form of the quantum impurity model and much of the rest of the report describes how to extract the coefficients of such a model from a CAD-level description of an EQI device. An experimental realization of our analog quantum simulation platform idea will need to be supplemented by a modeling tool that can convert the voltages supplied by an experimentalist into the particular quantum impurity model coefficients that will be realized. To this end, we added numerous new features to our in-house modeling tool, LACONIC. We note that EQIs can be realized in a wide variety of semiconductor quantum systems for which Sandia National Laboratories has fabrication and/or measurement proficiency, including electron quantum dots in the Si/MOS system, hole quantum dots in Ge/SiGe heterostructures, or dopant-based devices realized using ion implantation or APAM. We also note that LACONIC can be straightforwardly applied to any of these systems.

1.3. A quantum analog coprocessor for dynamical mean-field theory

While simulating a single quantum impurity model is itself a worthwhile goal, we are ultimately interested in augmenting the power of our EQI-based simulator by using it as an analog coprocessor for dynamical mean-field theory (DMFT) calculations. The basic theoretical concept underlying DMFT is that a particular family of instances of the infinite-dimensional Hubbard model can be mapped onto an Anderson impurity model [45, 46]. In other words, that we can replace a strongly correlated lattice model with a precisely chosen single impurity model. Rather than starting with a large array of EQIs, each of which needs to be characterized, controlled, and measured, we are instead interested in understanding whether we can control a *single* EQI and its coupling to a bath with sufficient control as to simulate many instances of the Anderson impurity model.

The identification between a strongly correlated lattice model and a single structured impurity model relies on achieving a form of self-consistency between the solutions to the two problems.

In particular, DMFT seeks the particular impurity model parameters such that the Green's function for the single impurity matches the on-site component of the lattice problem's Green's function [46, 47]. However, we do not have direct access to the lattice problem's Green's function otherwise we would not need this mapping. Consequently, one must verify self-consistency through a self-energy that relates the mean-field Green's function for the lattice problem to the impurity Green's function. This is further elaborated in Section 2.3.

Treating self-consistency as a condition that can be efficiently verified given the mean-field and impurity Green's functions, we see that the primary computational bottleneck of a DMFT calculation is solving the Anderson impurity model over and over again with different parameters until the self-consistent instance is found. In fact, it is the solution of the Anderson impurity model which is the classically difficult simulation task [48–50] that we are seeking to replace with our analog quantum simulator. We note that we are far from the first group to have such an idea, and that it was recently proposed to use a digital quantum computer to facilitate the solution of the Anderson impurity problem in a hybrid digital-quantum/digital-classical approach to DMFT [1]. However, this approach to DMFT will require the execution of algorithmic primitives that are likely to require quantum error correction to be successfully executed for non-trivial model systems. Thus we expect that the requisite quantum resources are far from being available, recalling the estimates for simulating the Fermi-Hubbard model described in Section 1.1.

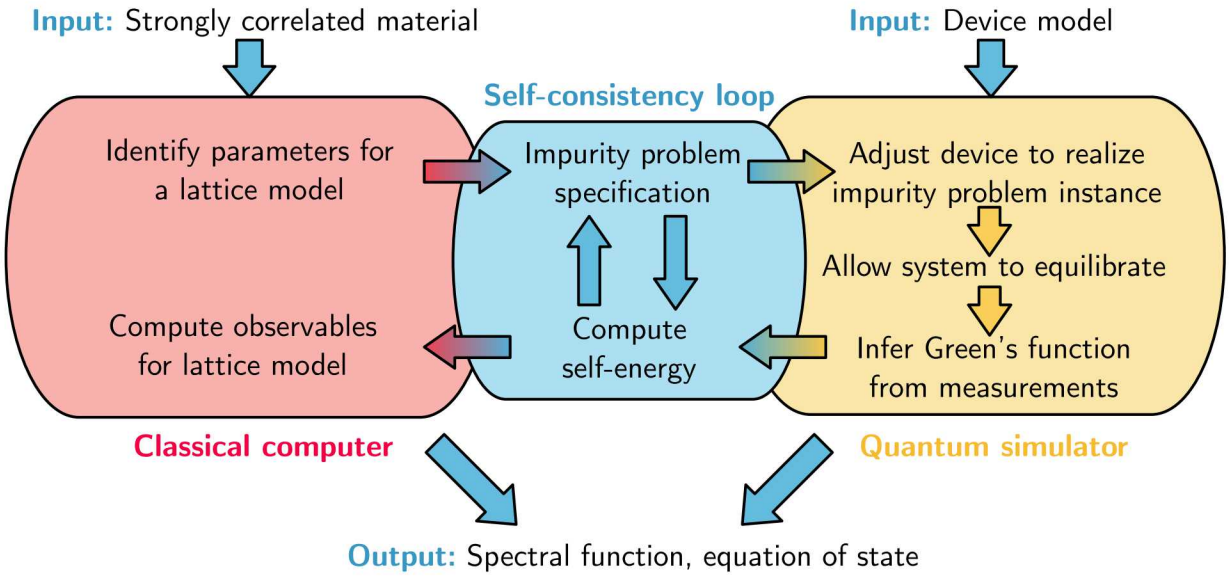

Figure 1-2 An overview of the hybrid analog-quantum/digital-classical approach to DMFT inspired by Ref. [1], particularly Fig. 1. Most of the technical details in this report are concerned with establishing a high-fidelity device model that can be used to reliably describe an analog quantum simulator based on various semiconductor EQI technologies.

Taking inspiration from Fig. 1 in Ref. [1], we provide a flowchart that summarizes our approach in Fig. 1-2. While we do not expect this approach to hybrid simulation to be as universal or as

powerful as an approach that uses a digital quantum computer[4], we hope that we can realize non-trivial demonstrations using devices that can already be fabricated and measured. Part of this hope is based on our prior observation that our simulator will have an effective Hilbert space dimension that is not only determined by the EQIs but the thermodynamically large baths to which they are coupled. Of course, we are not accessing the entire Hilbert space of this composite system but by realizing a strong coupling we still hope to expand the effective Hilbert space dimension of our simulator to be significantly larger than that of the EQIs alone.

We briefly reference recent progress in the state-of-the-art in hybrid quantum/classical approaches to DMFT since the publication of Ref. [1]. Given the focus of our project, we have not included a review of the vast literature on classical solvers for impurity models aside from prior citations to a few key articles. Two-site dynamical mean-field theory [51] has been investigated as a minimal example that might be realized on near-term quantum hardware [52]. While noise has been identified as a strong limiting factor to realizing a digital approach, particularly with respect to convergence of the self-consistency loop [53], clever compilation schemes promise to help mitigate some of these concerns [54]. Noise-resilient variational quantum approaches have also been implemented for the two-site problem [55], though the overall scalability of this approach to digital quantum simulation remains an open question. Finally, we note the recent development of a quasi-polynomial algorithm for efficiently solving the quantum impurity problem given in Ref. [56], which might be useful in efficiently preparing an approximation to the impurity model ground state on a quantum computer for use in a hybrid approach.

Most of the remaining technical work in this report is concerned with developing a high-fidelity device model that will enable analog quantum simulation of a wide variety of Anderson impurity model instances. Such a model is used to map from the voltages applied to the various gates in a hypothetical device to the Anderson impurity model coefficients that are realized. This is essential not only for controlling such an experiment but for *designing* one in the first place.

1.4. Summary of outcomes

The primary outcome of this project is a technical capability that is sufficient to both design and operate our proposed analog quantum coprocessor. This involved numerous advances to both modeling and theoretical capabilities that are summarized in this section. Among the secondary outcomes was a collaboration, enabled by this project, to study a first-of-its-kind EQI.

The primary modeling tool used to design and operate the proposed analog quantum coprocessor is LACONIC. Some of the highlights to advances to this modeling capability include:

- **A configuration interaction solver:** This was based on an approach that was originally developed for QCAD [57]. Novel features of the new approach include the use of an IP discretization of the Poisson equation to ennsure compatibility with the enriched basis sets

[4]Indeed, accelerating the DFT+DMFT approach that allows one to augment the accuracy of DFT calculations for arbitrary strongly correlated materials would require much more development of this idea and the associated technologies. This approach is reviewed in Ref. [47] and targeted in Ref. [1]. Here, we are strictly focused on taking the first steps of simulating strongly correlated lattice problems.

that are specific to LACONIC. This advance enables the evaluation of the $U_{\alpha\beta\gamma\delta}$ coefficient in Eq. 2a.

- **Support for modeling germanium hole devices:** This was done in synergy with other experimentally-driven projects. Both single- and multi-band models were developed and implemented.
- **Support for modeling APAM devices:** Adaptive hydrogenic basis functions were implemented to enable the study of dopant-based devices fabricated using APAM[5]. The mathematical details are preserved in Appendix A.
- **Implementation of Hardy space infinite elements [58]:** This allows us to describe scattering states in baths, as well as resonance states in EQIs. This advance enables the evaluation of the E_m and $V_{\alpha m}$ coefficients in Eqs. 2b and 2c.
- **Quantum transport through interacting regions:** The Meir-Wingreen formula for computing the current passing through an interacting region was implemented [59]. This advance enables us to predict the differential conductances that would be used in a bias spectroscopy measurement of one of our devices. While a capability for device-level transport modeling in quantum dots has been previously demonstrated using mean-field theory [60], the approach discussed in this report is an explicitly many-body approach that can capture Coulomb blockade.

Many of these advances are generically useful to both ongoing and prospective quantum device modeling efforts.

Other outcomes include more basic advances to our theoretical capabilities with highlights including:

- **Broader understanding of DMFT:** This isn't strictly limited to implementations on classical HPC systems and our own hybrid proposal, but approaches on NISQ and future fault-tolerant digital quantum hardware.
- **Resonances in EQIs:** We have a sharper perspective on the basic physics and mathematics associated with the theory of resonant states and non-Hermitian quantum mechanics. One outcome of this is a new perspective on the structure of many-body Hilbert spaces for open quantum systems in terms of biorthogonal systems.
- **New proficiency in non-equilibrium many-body theory:** Simulating transport measurements of an EQI coupled to a bath requires facility with non-equilibrium many-body theory to derive the relevant equations. We developed such a facility, culminating in the adaptation of our approach in terms of biorthogonal systems to a re-derivation of the Meir-Wingreen formula.

A final secondary outcome involved external collaborations enabled by this project. Members of the team were approached by collaborators at the University of New South Wales (UNSW) concerning a new type of EQI that had been experimentally realized and for which the theoretical description was still developing. Unlike the EQIs considered elsewhere in this report, the

[5] Of course, these methods also work equally well for single- or few-dopant devices fabricated using ion implantation.

quantum degrees of freedom were not individual electrons themselves but the spin of a single nucleus. In fact, the group at UNSW had for the first time coherently manipulated a single spin-7/2 nucleus, ^{123}Sb, implanted in a silicon nanoelectronic device. This project helped contribute to the theoretical understanding of this novel EQI technology, for which the results are reported in Ref. [61].

2. THEORY

We first state the precise form of the second-quantized quantum impurity model and the first-quantized low-energy effective theory that we use to model EQIs in Section 2.1. We next provide a brief overview of Green's functions to describe the key quantities of interest in analog quantum simulation of DMFT in Section 2.2. Finally, we describe the self-consistency condition that is used to relate the properties of a single impurity to those of a lattice of impurities in Section 2.3.

2.1. Quantum impurity models and low-energy effective theories

The key observation that inspires our approach is that a system of one or a few EQIs coupled to a bath are a natural realization of a tunable quantum impurity model. Generically, the second-quantized quantum impurity model Hamiltonian takes the following additive three-term form,

$$\hat{H} = \hat{H}_i + \hat{H}_b + \hat{H}_{i-b}, \tag{1}$$

in which

$$\hat{H}_i = \sum_{\alpha}^{N_i} \varepsilon_\alpha \hat{a}_\alpha^\dagger \hat{a}_\alpha + \sum_{\alpha,\beta}^{N_i} t_{\alpha\beta} \hat{a}_\alpha^\dagger \hat{a}_\beta + \sum_{\alpha,\beta,\gamma,\delta}^{N_i} U_{\alpha\beta\gamma\delta} \hat{a}_\alpha^\dagger \hat{a}_\beta^\dagger \hat{a}_\gamma \hat{a}_\delta, \tag{2a}$$

$$\hat{H}_b = \sum_{m}^{N_b} E_m \hat{b}_m^\dagger \hat{b}_m, \text{ and} \tag{2b}$$

$$\hat{H}_{i-b} = \sum_{\alpha,m}^{N_i,N_r} V_{\alpha m} \hat{a}_\alpha^\dagger \hat{b}_m + \overline{V}_{\alpha m} \hat{b}_m^\dagger \hat{a}_\alpha. \tag{2c}$$

The three terms are respectively the impurity (H_i), bath (H_b), and coupling (H_{i-b}) Hamiltonians. The impurity consists of N_i localized orbitals with single-particle energies ε_α, between which there is a tunneling energy $t_{\alpha\beta}$ and a mutual Coulomb repulsion energy $U_{\alpha\beta\gamma\delta}$. The bath consists of N_b delocalized fermionic modes with single-particle energies E_m. The impurity and bath are coupled such that orbital α and mode m can exchange a particle with a rate proportional to the modulus of $V_{\alpha m}$. The operator $\hat{a}_\alpha$ ($\hat{a}_\alpha^\dagger$) annihilates (creates) one flavor of fermion in orbital α of the impurity and the operator $\hat{b}_m$ ($\hat{b}_m^\dagger$) creates (annihilates) a distinct flavor of fermion in mode m

of the bath. The two flavors of fermions are mutually distinguishable but otherwise obey the canonical anticommutation relations within a given flavor,

$$\{\hat{a}_\alpha, \hat{a}_\beta\} = \{\hat{b}_m, \hat{b}_n\} = 0, \tag{3a}$$

$$\{\hat{a}^\dagger_\alpha, \hat{a}^\dagger_\beta\} = \{\hat{b}^\dagger_m, \hat{b}^\dagger_n\} = 0, \tag{3b}$$

$$\{\hat{a}_\alpha, \hat{a}^\dagger_\beta\} = \delta_{\alpha\beta}, \text{ and } \{\hat{b}_m, \hat{b}^\dagger_n\} = \delta_{mn}. \tag{3c}$$

To develop an EQI-based quantum simulation platform for this model, it is necessary to also define a first-quantized low-energy effective theory of the analog quantum simulator itself. This allows us to develop a device model from which we can extract the coefficients in Eq. 1 given the operating conditions of the simulator. One such theory is effective mass theory, which has previously been applied to model donor atom [62] and quantum dot [63] EQIs in silicon. Effective mass theory allows us to express the first-quantized Hamiltonian for N_p particles in an EQI system as

$$H(\mathbf{r}_1, \ldots, \mathbf{r}_{N_p}) = \sum_{i=1}^{N_p} \left(-\frac{\nabla^2_{\mathbf{r}_i}}{2m^*} + V_{ext}(\mathbf{r}_i) \right) + \sum_{i \neq j}^{N_p} \frac{e^2}{4\pi\varepsilon|\mathbf{r}_i - \mathbf{r}_j|}, \tag{4}$$

where the first term is the kinetic energy renormalized by the effective mass, m^*, the second term is the interaction of each carrier with an externally-impressed electrostatic potential (e.g., due to the control electrodes and/or built-in potential in the heterostructure), and the third term is due to the Coulombic repulsion between carriers, screened by the bulk dielectric constant of the host material, ε. We note that there are a few subtleties that we are eliding for brevity. First, generally the effective mass is a tensor quantity. Second, it is often the case that there are internal quantum numbers that are also relevant to the physics, e.g., the valley index for electrons in silicon devices or the light-hole/heavy-hole band index in germanium quantum wells. We will proceed by simply asserting that we know how to incorporate these platform-specific details.

Thanks to the interaction term in Eq. 4, the problem of finding the Hamiltonian's lowest energy eigenstates is generically computationally intractable[6]. However, one can apply mean-field theory (e.g., Hartree-Fock or density functional theory) to approximate the ground state of Eq. 4, and a basis for a many-body Hilbert space that could be used to instantiate Eq. 1.

We describe the numerical solution of Eq. 4 and the extraction of the impurity model parameters in more detail in Section 3. For now it suffices to state the overall workflow:

1. A CAD-level design of the EQI device is specified in terms of the composition of the material stack and the dimensions and relative positions of the electrostatic gates.

2. This description of the device is used to specify a semiclassical electrostatics model (e.g., Thomas-Fermi theory [60, 65]) that defines $V_{ext}(\mathbf{r})$ as a function of the experimental control voltages.

[6] Generically, the problem of finding the ground state of an algebraically local Hamiltonian is related to a QMA-COMPLETE decision problem [64]. This is roughly the quantum equivalent of NP-COMPLETE, in which a quantum proof can be efficiently verified by a quantum computer but it is unlikely that a quantum computer can find the proof without further restrictions.

3. A region of space around the EQI and bath are isolated from the electrostatics model and an instance of Eq. 4 is posed, using mean-field theory to approximate the interaction term. The associated eigenproblem is solved, yielding the single particle orbitals associated with the creation and annihilation operators.

4. The coefficients of Eq. 1 are extracted. Repeated solutions for different voltages can be used to study the space of realizable parameters for design purposes. This can also be used to simulate measurements on the analog quantum simulator for the purposes of calibration and, eventually, operation.

Next, we introduce one of the key theoretical abstractions that is needed to connect analog quantum simulation of a single quantum impurity to a lattice of impurities.

2.2. Green's functions

There are two contexts in which Green's functions are relevant to our aims. The first is as a central quantity in DMFT, through which the properties of a single quantum impurity are related to the properties of a lattice of quantum impurities. The other is in simulating transport experiments that could be used to design or operate the analog quantum coprocessor platform proferred in this report. We begin by referring the reader to Refs. [66–68] for textbooks with excellent discussions on the Green's function in the context of many-body theory.

The term "Green's function" appears elsewhere in physics in the context of solving inhomogeneous linear partial differential equations [69]. In that context, Green's functions encode the inverse of the linear operator defining a partial differential equation and the constraints that specify the initial and/or boundary conditions needed for its unique solution. The Green's function can be convolved with the inhomogeneous term to yield the solution to arbitrary instances of the partial differential equation. Noting that most of the equations that we care about in quantum many-body theory are nonlinear due to the presence of interactions, the use in this context is slightly more expansive. In particular, they are useful in perturbatively treating interactions and/or in constructing and closing infinite hierarchies of equations for many-body problems. It is only in the particular limit of a non-interacting problem that the two-point Green's function corresponds to the "classic" use.

To define the Green's functions that we are interested in, we first need to define a transformation that relates operators defined in the Schrödinger picture to those in the Heisenberg picture. This is no different than the usual presentation in introductory quantum mechanics in which one has a choice between assigning the dynamics of a system to the state of a quantum system or its observables [70]. The Heisenberg picture annihilation operator for an arbitrary EQI orbital is defined as,

$$\hat{a}_{H,\alpha}(t) = e^{i\hat{H}t}\hat{a}_{\alpha}e^{-i\hat{H}t}, \tag{5}$$

where $\hat{H}$ is the system Hamiltonian and t is time. It is evident that this operator obeys the so-called Heisenberg equation of motion,

$$i\frac{d}{dt}\hat{a}_{H,\alpha}(t) = \left[\hat{a}_{H,\alpha}(t), \hat{H}\right], \tag{6}$$

where extensions to the creation operator, bath operators, or arbitrary products thereof, should be evident. We will henceforth suppress the subscripted H on Heisenberg operators and assume that the existence of a temporal argument is enough to distinguish it from its Schrödinger picture counterpart. Being a first order differential equation, given an initial condition on $\hat{a}_\alpha(t)$, e.g., $\hat{a}_\alpha(0) = \hat{a}_\alpha$, there exists a unique solution to Eq. 6.

The n-particle Green's functions are related to expectation values of particular ordered products of $2n$ single-particle Heisenberg operators with respect to some known state (e.g., the ground state or an equilibrium thermal state). The ordering of the constituent creation and annihilation operators distinguishes different types of Green's functions, which correspond to functions whose Fourier transforms are analytic on different portions of the complex plane[7]. As we will see later, the region of the complex plane over which one of these functions is analytic encodes information about the boundary conditions in the physical system and the causal structure of the operator product.

For the purposes of DMFT the particular Green's function of interest is the time-ordered 1-particle Green's function of the impurity,

$$G_{\alpha\beta}(t) = -i\langle\Psi_0|\mathcal{T}\left[\hat{a}_\alpha(t)\hat{a}^\dagger_\beta(0)\right]|\Psi_0\rangle, \tag{7a}$$

$$= -i\langle\Psi_0|\theta(t)\hat{a}_\alpha(t)\hat{a}^\dagger_\beta(0) - \theta(-t)\hat{a}^\dagger_\beta(0)\hat{a}_\alpha(t)|\Psi_0\rangle \tag{7b}$$

where $\mathcal{T}$ is the time-ordering operator, which is defined explicitly in the second line. We note that this Green's function is itself a $N_i \times N_i$-matrix-valued function of time, in so far as α and β index $\{1,\ldots,N_i\}$. Intuitively, this Green's function is a matrix of amplitudes associated with the impurity returning to its initial state after a time t elapses between adding a fermion to a specific orbital and removing a fermion from a potentially distinct orbital. For positive times the added/removed fermion is a particle and for negative times it is an antiparticle[8]. We note that we will suppress the α and β subscripts and add a carat when referring to the 1-particle Green's function independent of a particular basis for the single-particle Hilbert space, i.e., $G_{\alpha\beta}(t) \to \hat{G}(t)$

The Fourier transform of the Green's function in Eq. 7 is analytic in neither the upper nor lower half of the complex plane. Instead we often work with the retarded (R) and advanced (A) Green's functions, the Fourier transforms of which are so distinguished,

$$G^R_{\alpha\beta}(t) = -i\theta(t)\langle\Psi_0|\{\hat{a}_\alpha(t), \hat{a}^\dagger_\beta(0)\}|\Psi_0\rangle, \text{ and} \tag{8a}$$

$$G^A_{\alpha\beta}(t) = i\theta(-t)\langle\Psi_0|\{\hat{a}_\alpha(t), \hat{a}^\dagger_\beta(0)\}|\Psi_0\rangle. \tag{8b}$$

Here it is evident that $G_{\alpha\beta}(t)$ can be reconstructed from $G^R_{\alpha\beta}(t)$ and $G^R_{\alpha\beta}(t)$. Physically, these functions are all ultimately related to the density of single particle excitations which one can imagine measuring in the time or frequency domain through, e.g., charge sensing or bias spectroscopy.

[7] More specifically, we are referring to the extensions of the Fourier transforms evaluated on the real line onto the complex plane.

[8] Here we specifically refer to particles and antiparticles because the particles in a hole-based device are holes and the antiparticles are electrons. Of course, one could reverse this convention with care.

From the 1-particle Green's function one can compute many properties of the reference state, including the expectation value of any single-particle operator, the energy of the reference state, and the spectrum of excitations [66]. Of course, if one had direct access to $|\Psi_0\rangle$, these same properties would be accessible but at the expense of needing to work with a state vector whose dimension scales exponentially in N_i and N_b. The primary advantage to working with $G_{\alpha\beta}(t)$ is that it is a lower-dimensional object. Thus, given an initial condition $G_{\alpha\beta}(t = t_i)$, one can imagine writing the equation of motion for $G_{\alpha\beta}$ and time evolving to solve for $G_{\alpha\beta}(t)$ at arbitrary times. This equation of motion is

$$i\frac{d}{dt}G_{\alpha\beta}(t) = \delta(t)\delta_{\alpha\beta} + \langle\Psi_0|\theta(t)\left[\hat{a}_\alpha(t),\hat{H}\right]\hat{a}_\beta(0) - \theta(-t)\hat{a}^\dagger_\beta(0)\left[\hat{a}_\alpha(t),\hat{H}\right]|\Psi_0\rangle, \tag{9}$$

where we quickly find that the second term on the right-hand side generally leads to an infinite hierarchy of equations of increasing dimensionality [68]. In the specific case of the Hamiltonian in Eq. 1, there are two major complications. The first is that the quartic term due to on-site interactions in H_i couples the 1-particle Green's function to the 2-particle Green's function. The equation of motion for the 2-particle Green's function depends on the 3-particle Green's function, and so on. The second is that H_{i-b} gives rise to terms that couple in $n-$point correlations over the entire system, including the bath. This obviates the utility of working with a Green's function localized to the EQI by increasing the dimensionality of Green's functions to accommodate the dimensionality of the bath. In fact, these two complications compound one another. Thus, one of the central challenges in quantum many-body theory is arriving at approximate closures to hierarchies like this that are both accurate and physically sensible, e.g., they obey the same conservation laws as the many-body system.

In addition to providing a heuristic description of the most basic elements of the many-body Green's function formalism, this description should highlight the computational difficulty of solving for $G_{\alpha\beta}(t)$, which is itself a seemingly simple pathway to understanding many of the interesting properties of a system described by the Hamiltonian in Eq. 1. Accordingly, the ability to either make direct or indirect measurements of $G_{\alpha\beta}(t)$ in a highly tunable EQI is a computationally powerful capability. We next consider the manner in which DMFT allows us to relate the properties of a single EQI hybridized with a particular bath to the properties of a lattice of EQIs representative of, e.g., a strongly correlated material.

2.3. Relating a single impurity and a lattice of impurities

The contents of this section related to self-consistency make use of many well-established relationships from the literature on DMFT [1, 46, 47]. The central premise of DMFT is that we can study the properties of a strongly correlated lattice model through the properties of a proxy system governed by Eq. 1. Such a strongly correlated lattice model might be, e.g., the Fermi-Hubbard model for which DMFT was first developed [45], but the idea is more general than that particular model. We simply require that each site obey a Hamiltonian of the form in Eq. 2a with the connectivity of the sites and their coupling remaining arbitrary. It is evident that the standard Fermi-Hubbard model would correspond to a single-site impurity Hamiltonian in which $N_i = 2$, and the two orbitals correspond to opposite spins that are uncoupled, i.e., $t_{1,2} = 0$.

Because of this generality, we will remain agnostic to the particular instance of the lattice Hamiltonian and simply assert that we are interested in the properties of some unspecified $\hat{H}_{latt}$. We assume that $\hat{H}_{latt}$ has some non-interacting or mean-field limit, $\hat{H}_{latt,0}$ that is efficiently computable and for which there exist good quantum numbers, $\mathbf{k}$, related to the discrete translation invariance of the lattice. As indicated in Fig. 1-1, the lattice model and the single impurity model are identified with one another when their Green's functions are equal,

$$G_{latt,\alpha\beta}(\omega) = G_{\alpha\beta}(\omega),\ \forall \alpha,\beta \in \{1,\ldots,N_i\}, \tag{10}$$

where G_{latt} is defined with respect to Heisenberg evolution by $\hat{H}_{latt}$ in Eq. 8a, and we have taken the Fourier transform of both Green's functions. We have chosen to work in the Fourier domain to facilitate practically achieving this condition. In fact, the self-consistency condition will be verified for N_M imaginary values of ω, Matsubara frequencies,

$$\omega_{n,M} = i(2n+1)\pi T,\ \forall n \in \{1,\ldots,N_M\}, \tag{11}$$

where T is the electronic temperature. Given an estimate of $G_{\alpha\beta}(\omega)$ at real frequencies from either a direct frequency-domain measurement or a real-time measurement of the EQI, one can compute the Green's function at the Matsubara frequencies by way of a Hilbert transform.

Thus the primary technical challenge of relating the properties of a single EQI to a target lattice impurity problem becomes that of finding the coefficients in Eq. 2b and Eq. 2c for which a measurement of a single EQI realizing that Hamiltonian satisfies Eq. 10 for a particular instance of $\hat{H}_{latt}$ at the N_M Matsubara frequencies. Of course, we have no easy way to compute or measure $G_{latt,\alpha\beta}(\omega)$ or else we would not need DMFT. To arrive at a scheme for approximating $G_{latt,\alpha\beta}(\omega)$ such that we can compute it using $G_{\alpha\beta}(\omega)$, we need to define the notion of a self-energy. Intuitively, the self-energy is an operator that captures the difference between a local sector of a non-interacting Hamiltonian and an interacting version of that Hamiltonian that is coupled to the rest of the universe. For the lattice problem, the self-energy is given as

$$\hat{\Sigma}_{latt}(\mathbf{k},\omega_n) = \hat{G}^{-1}_{latt,0}(\mathbf{k},\omega_n) - \hat{G}^{-1}_{latt}(\mathbf{k},\omega), \tag{12}$$

where $\hat{G}_{latt,0}$ is the efficiently computable Green's function for $\hat{H}_{latt,0}$ and we have introduced a dependence on $\mathbf{k}$, the good quantum numbers for $\hat{H}_{latt,0}$. The two Green's functions are then defined as

$$\hat{G}_{latt,0}(\mathbf{k},\omega_n) = \left[(\omega_n+\mu)\hat{1} - \hat{H}_{latt,0}(\mathbf{k})\right]^{-1} \text{ and} \tag{13a}$$

$$\hat{G}_{latt}(\mathbf{k},\omega_n) = \left[(\omega_n+\mu)\hat{1} - \hat{H}_{latt,0}(\mathbf{k}) - \hat{\Sigma}_{latt}(\mathbf{k},\omega_n)\right]^{-1}, \tag{13b}$$

where Eqs. 12 and 13a are sufficient to derive Eq. 13b. Noting that we cannot easily compute $\hat{\Sigma}_{latt}$ either, we approximate it with a local self-energy, $\hat{\Sigma}_{latt}(\mathbf{k},\omega_n) \approx \hat{\Sigma}(\omega_n)$ in Eq. 13b,

$$\hat{G}_{latt}(\mathbf{k},\omega_n) \approx \left[(\omega_n+\mu)\hat{1} - \hat{H}_{latt,0}(\mathbf{k}) - \hat{\Sigma}(\omega_n)\right]^{-1}, \tag{14}$$

where $\hat{\Sigma}(\omega_n)$ is the self-energy for the single impurity problem.

The DMFT consistency condition in Eq. 10 can then be rewritten as

$$\hat{G}(\omega_n) = \hat{G}_{latt}(\mathbf{k}=0,\omega_n) = \left[(\omega_n+\mu)\hat{1} - \hat{H}_{latt,0}(\mathbf{k}=0) - \hat{\Sigma}(\omega_n)\right]^{-1}. \tag{15}$$

To satisfy this condition in practice, an iterative procedure can be applied:

1. Index each iteration by an integer, j.

2. Guess $\hat{\Sigma}_{j=0}(\omega_n)$ for the first iteration.

3. Execute the following for each $j = 1, \ldots$ until convergence is reached, quantified by an error tolerance ε_{tol}.

   a) Compute $\hat{G}_{j,latt}(\mathbf{k} = 0, \omega_n)$ from $\hat{\Sigma}_j(\omega_n)$.

   b) Compute the single impurity model parameters $\{\varepsilon_\alpha, V_{\alpha m}\}_j$ for Eq. 1 that are consistent with $\hat{G}_{j,latt}(\mathbf{k} = 0, \omega_n)$.

   c) Using the low-energy effective theory in Eq. 4, find voltages that realize $\{\varepsilon_\alpha, V_{\alpha m}\}_j$ in the EQI-based analog quantum simulator.

   d) Infer $\hat{G}_j(\omega_n)$ from measurements of the EQI-based analog quantum simulator.

   e) Check whether $||\hat{G}_j(\omega_n) - \hat{G}_{j-1}(\omega_n)|| < \varepsilon_{tol}$.

   f) If convergence has been reached, exit loop.

   g) Otherwise, compute $\hat{\Sigma}_{j+1}(\omega_n)$ and go to a.

4. Extract physical properties from $\hat{G}_{j,latt}$ calculated using $\hat{\Sigma}_j$.

The above self-consistency procedure makes it clear that we can augment the computational power of an analog quantum simulator for a single quantum impurity by leveraging it as the impurity solver within a DMFT loop, allowing us to study lattices of such impurities. The key technical advances that are required are then a sufficiently high-fidelity model of the EQI-based analog quantum simulator that we can realize a particular instance of Eq. 1 on the fly. The remainder of this report is primarily concerned with establishing such a high-fidelity model and future work will see its continued use in designing and demonstrating this approach to analog quantum simulation.

3. NUMERICAL TOOLS

The numerical solution of the low-energy effective theory in Eq. 4 using the LACONIC software package is described in Section 3.1. The use of the Hardy space method to represent states in the EQI and bath is described in Section 3.2, introducing the need for biorthogonal systems to discretize non-Hermitian operators. We then briefly describe the use of LACONIC to extract the Hamiltonian coefficients in Eq. 1 in Section 3.3, providing the particular example of a Ge hole EQI. Finally, we derive a biorthogonal version of the Meir-Wingreen formula [59] for transport through an interacting system in Section 3.4, demonstrating its utility in simulating the types of transport measurements that may be used to infer the single impurity Green's function in our analog quantum simiulator.

3.1. Numerical solution of the low-energy effective theory

To model the behavior of our analog quantum simulator, we make use of the LACONIC software package to solve Eq. 4 for a potential landscape, $V_{ext}(\mathbf{r})$, derived from a semiclassical electrostatics model solved in COMSOL [71]. The particular details of the semiclassical electrostatic model vary from platform to platform, but we typically use a 2D Thomas-Fermi model to govern charge accumulation at the interfaces at which we expect the bath states to accumulate, while constraining the region corresponding to the EQIs to have no accumulation. To generate the single-particle orbitals, energies, and other coefficients, we typically start with a self-consistent mean-field approximation to Eq. 4 in which

$$H(\mathbf{r}_1,\mathbf{r}_2,\ldots,\mathbf{r}_{N_p}) = \sum_{i=1}^{N_p}\left(-\frac{\nabla^2_{\mathbf{r}_i}}{2m^*} + V_{ext}(\mathbf{r}_i) + V_{mf}\left[n(\mathbf{r})\right](\mathbf{r}_i)\right), \text{ such that} \tag{16a}$$

$$n(\mathbf{r}) = \int d\mathbf{r}_2 d\mathbf{r}_3 \ldots d\mathbf{r}_{N_p} |\Psi(\mathbf{r}_1,\mathbf{r}_2,\ldots,\mathbf{r}_{N_p})|^2, \text{ and} \tag{16b}$$

$$V_{mf}\left[n(\mathbf{r})\right](\mathbf{r}) = V_H\left[n(\mathbf{r})\right](\mathbf{r}) + V_{xc}\left[n(\mathbf{r})\right](\mathbf{r}), \text{ where} \tag{16c}$$

$$\nabla\cdot(\varepsilon\nabla V_H(\mathbf{r})) = n(\mathbf{r}), \tag{16d}$$

and $V_{xc}\left[n(\mathbf{r})\right]$ is a suitable density functional approximation to electronic exchange and correlation. This ultimately leads to the need to self-consistently solve an eigenproblem of the form

$$\left(-\frac{\nabla^2}{2m^*} + V_{ext}(\mathbf{r}) + V_{mf}\left[n(\mathbf{r})\right](\mathbf{r})\right) F_\alpha(\mathbf{r}) = \varepsilon_\alpha F_\alpha(\mathbf{r}),\ \forall\alpha\in\{1,\ldots,N_i\}, \tag{17}$$

where

$$n(\mathbf{r}) = \sum_{\alpha=1}^{N_i} f\left[\mu,T_e\right](\varepsilon_\alpha)|F_\alpha(\mathbf{r})|^2 \tag{18}$$

in which $f\left[\mu,T_e\right](\varepsilon_\alpha)$ is the Fermi-Dirac distribution, T_e is the electronic temperature, μ is the chemical potential of the EQI at zero bias, and ε_α are the single particle energies from Eq. 2a. This is the central problem that LACONIC solves.

LACONIC is based on an interior penalty [72, 73] discontinuous Galerkin discretization [74] of Eq. 17. It does so using a mesh-based representation of the problem domain, with the flexibility to handle tetrahedral, quadrilateral, triangular, and linear elements - with support for hexahedral elements being finalized near the end of this project. The key reason for using a discontinuous Galerkin discretization is to allow for the local enrichment of the function spaces used to represent the solution of Eq. 17 in the vicinity of regions with known physics [75]. Dopant-based devices fabricated using APAM provide the strongest motivation for this. In such devices, each individual dopant or clusters thereof produces a Coulomb singularity in $V_{ext}(\mathbf{r})$. This produces a cusp in $F_\alpha(\mathbf{r})$ that requires significant adaptation to resolve when exclusively using conventional compactly supported polynomial basis functions. One of the advances in this project was the development of anisotropic atomic orbitals that can be used to locally augment such basis functions with linear combinations of hydrogenic orbitals to appropriately capture the anisotropy of the effective mass. Some of the details of the basis, including a subset of the necessary integrals, are given in Appendix A. Other areas that require enrichment of the local function space

include the accurate representation of the evanescent tail of a wave function penetrating a potential barrier at a material interface and in the description of bath states, as described in Section 3.2.

To solve Eq. 17, we begin with a restriction of the problem domain to $\Omega \subset \mathbb{R}^d$ with boundary $\partial\Omega$. Ω is tesselated by N_e tetrahedral or hexahedral elements, $\{T_e | e \in \{1,\ldots,N_e\}$, where the ith element has boundary ∂T_i. The envelope function is then approximated as

$$F_\alpha(\mathbf{r}) \approx \sum_{e=1}^{N_e} \sum_{p=1}^{N_p(e)} c_{\alpha,e,p} f_{e,p}(\mathbf{r}), \tag{19}$$

where $c_{\alpha,e,p}$ are the unknown coefficients to be resolved for the αth eigenvector of Eq. 17 and $f_{e,p}(\mathbf{r})$ is the pth basis function with support restricted to the eth element. We are careful to use a notation in which the number of basis functions per element is explicitly dependent on the index of the element. The fact that the local basis functions can change from element to element is one of the key features that we are seeking to leverage.

In the interior penalty discretization scheme used in LACONIC, the eigenproblem in Eq. 17 is rendered as a finite-dimensional linear system of equations, one row for each basis function. The row corresponding to $f_{e',p'}(\mathbf{r})$ is

$$\sum_{e,p} c_{\alpha,e,p} \Bigg(\frac{1}{2m^*} \big(\langle \nabla f_{e',p'}, \nabla f_{e,p} \rangle_{T_e} - \langle \{\{\nabla f_{e',p'}\}\}, [[f_{e,p}]] \rangle_{\partial T_e} - \langle [[f_{e',p'}]], \{\{\nabla f_{e,p}\}\} \rangle_{\partial T_e} \cdots$$
$$\cdots + \beta(T_e) \langle [[f_{e',p'}]], [[f_{e,p}]] \rangle_{\partial T_e} \big) + \langle f_{e',p'}, \left(V_{ext} + V_{mf}\right) f_{e,p} \rangle_{T_e} \Bigg) = \varepsilon_\alpha \sum_{e,p} c_{\alpha,e,p} \langle f_{e',p'}, f_{e,p} \rangle_{T_e}, \tag{20}$$

where $\langle \cdot,\cdot \rangle_{T_e}$ denotes an inner product over T_e, $\langle \cdot,\cdot \rangle_{\partial T_e}$ denotes an inner product over ∂T_e, $\beta(T_e)$ is a positive real penalty factor that is scaled by the area of the interface, $[[.]]$ is the jump operator, and $\{\{.\}\}$ is the average operator - both of which accommodate the discontinuous representation of the solution across elements [75]. LACONIC assembles a sparse matrix by aggregating Eq. 20 for each basis function and the resulting eigenproblem is solved using the Locally Optimal Block Preconditioned Conjugate Gradient (LOBPCG) method [76]. The solutions to Eq. 20 are a discrete representation of single-particle orbitals that span a Hilbert space that can be used to generate many-particle states through association with the creation and annihilation operators in Section 2.1. By postprocessing solutions to Eq. 20 we can then generate the coefficients to Eq. 1, as we will discuss in Section 3.3. First, however, we discuss a novel aspect of studying EQIs that are strongly coupled to baths and that is the representation of bound, quasi-bound, and unbound states.

3.2. Representing the quantum impurity and bath

One of the primary technical challenges in creating a detailed device-level model for an EQI that is strongly coupled to a structured electronic bath is the representation of the extended states in the bath and their coupling to bound states in the EQI. Even more subtle is the representation of

quasi-bound states in which the partition between the extent of the state on the impurity and in the bath is blurred due to strong hybridization. Here, the problem can be more abstractly articulated as finding a basis for the Hilbert space of single-particle states in the bath, with infinite extent and satisfying the appropriate asymptotic boundary conditions. Hardy space methods offer one solution.

The general class of Hardy space methods for open systems has seen wide application in applied mathematics [58, 77–81] and there has even been a demonstration relevant to transport in nanoelectronic devices [82]. The central concept underlying all of these methods is the fact that the space of square integrable functions on some domain admits an orthogonal decomposition into two spaces of square integrable functions that obey either incoming or outgoing asymptotic boundary conditions. These two spaces are Hardy spaces, which are spaces of holomorphic functions with boundary values that obey particular conditions. When equipped with an appropriate inner product they are themselves Hilbert spaces that individually span state spaces describing incoming and outgoing particles.

We consider a single spinless particle, the properties of which are completely specified by its position, $\mathbf{r}$, in a domain, $\Omega \subset \mathbb{R}^d$. We are particularly interested in the specific case in which $\Omega = \Omega_{int} \cup \Omega_{ext}$, where Ω_{int} in an interior domain with finite extent (e.g., a region containing EQIs), and Ω_{ext} is an exterior domain with infinite extent (e.g., the baths to which the EQIs are coupled). The two subdomains have N_Γ boundaries between them, $\{\Gamma_i | i \in 1 \ldots, N_\Gamma\}$, and we would like to construct a particular partitioning of the Hilbert space for states in Ω_{ext} that differentiate between states that describe an incoming particle entering Ω_{int} and outgoing particles leaving Ω_{int}. This differentiation can be achieved using the Hardy space method, and we draw heavily from Ref. [58] in describing it.

The key technical consideration for the Hardy space method is the so-called "pole condition" that relates the asymptotic properties of states to their analytic behavior. Simply put, the meromorphic extension of the Laplace transform of incoming and outgoing states for a transform variable conjugate to a radial coordinate normal to Γ_i are analytic on different halves of the complex plane. We define such a radial coordinate as r and ignore any dependencies in transverse directions for simplicity, the conjugate transform variable is s. The Laplace transform, $\mathcal{L}$, of an arbitrary function of r, $f(r)$, is given as

$$(\mathcal{L}f)(s) = \int_0^\infty dr\, e^{-sr} f(r). \tag{21}$$

The Hilbert spaces of functions for which the extensions of $(\mathcal{L}f)(s)$ to $\mathbb{C}$ are analytic on the upper and lower halves of the complex plane form an orthogonal decomposition of the full Hilbert space. The two halves of this decomposition correspond to incoming and outgoing states. By constructing a basis for either of these two subspaces, we can represent functions that are strictly incoming or strictly outgoing.

We can also apply another transform, subsequent to the Laplace transform, to render the pole condition in terms of analyticity on the interior or exterior of the complex unit disc. A basis for functions that are analytic on the interior of the complex unit disc is particularly straightforward,

consisting simply of monomials in the transform variable, z. The transform that accomplishes the desired mapping is the Möbius transform,

$$(\mathcal{M}_{k_0} f)(z) = \sqrt{-2ik_0}(f \circ m_{k_0})(z)\frac{1}{z-1}, \text{ where} \tag{22a}$$

$$m_{k_0}(z) = ik_0\frac{z+1}{z-1}, \tag{22b}$$

and we have chosen the $\sqrt{-2ik_0}$ prefactor to ensure unitarity. In fact, the Möbius transform is a family of transforms parametrized by $k_0 \in \mathbb{C}$, where the notation k_0 is intended to evoke a physical wave number. This will be relevant in its application to studying scattering and quasi-bound state problems.

In Ref. [58] and subsequent work, the choice of the Laplace-Möbius transform is convenient because it converts a straightforward formulation of the Helmholtz eigenproblem from being quadratic in the wave number to one that is linear in the wave number. Additionally the matrix elements take on a particularly simple form thanks to the monomial basis in the transform variable. In this project, we have chosen to investigate the Hardy space method to assess whether it is a more economical basis than others for representing EQI states that are strongly coupled to the bath states. Similarly the infinite element framework that we have added to LACONIC can be easily extended to other basis functions.

For many of our derivations and because we are working with a Helmholtz-like equation with non-constant coefficients (i.e., Eq. 17), we have found it more convenient to work directly with the eigenfunctions of the Laplace-Möbius transform in the untransformed variable. These eigenfunctions are

$$u_m(r) = \sqrt{-2ik_0}e^{-ik_0 x}L_n(-2ik_0 r) \tag{23}$$

where L_m is the mth Laguerre polynomial, and $\mathrm{Re}\{k_0\} > 0$ and $\mathrm{Im}\{k_0\} < 0$ ensures that these eigenfunctions describe the desired set of quasi-bound states. Such a basis has been implemented in LACONIC using the interior penalty formulation in the previous section. We have verified our implementation for scattering, quasi-bound, and bound state problems relevant to EQI modeling, with exemplary results in Fig. 3-1.

In the course of our implementing the Hardy space method we came across a curious feature. The basis functions in Eq. 23 are not orthogonal in the usual sense as complex conjugation maps between Hardy spaces that satisfy different asymptotic boundary conditions. Instead, the orthogonality relation holds *without* complex conjugation. In order for the usual inner product to hold for the evaluation of matrix elements, we then need to define a biorthogonal system in which the dual basis to the one in Eq. 23 are the complex conjugates to those functions.

One consequence of this is in the construction of matrix elements in Eq. 20, where we must now be careful to use the Hardy space basis and its dual. While this might seem to be a simple substitution, it ultimately means that self-adjoint operators will no longer necessarily generate Hermitian matrices. Another more subtle consequence is that we must revise the usual fermionic operator algebra to accommodate the creation of many-body states that respect the Hardy space formalism. We will illustrate this with an explicit construction in our re-derivation of the Meir-Wingreen formula in Section 3.4.

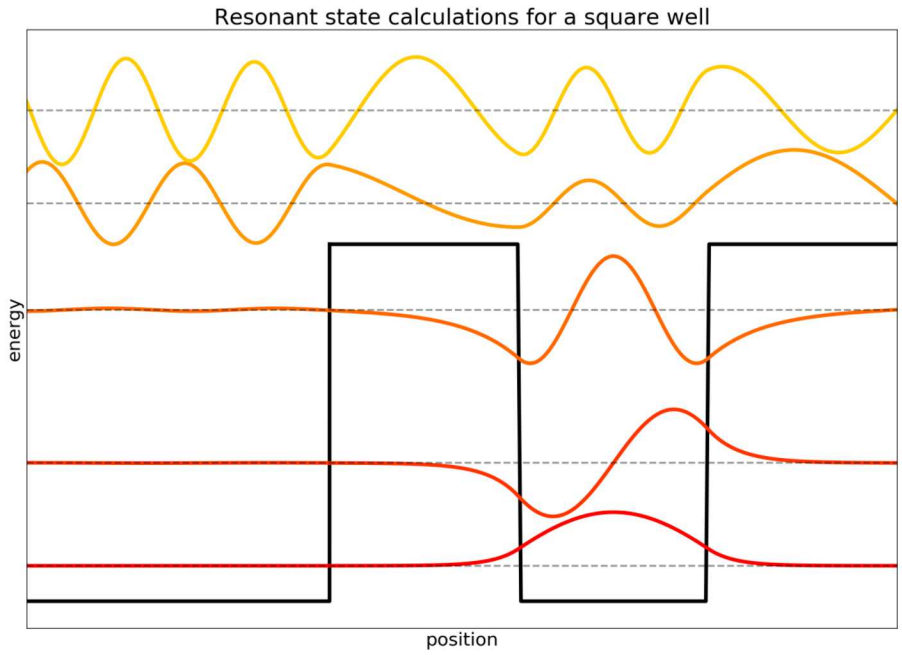

Figure 3-1 Numerical verification of the Hardy space method for an analytically tractable one-dimensional finite square well. The wave functions for exemplary bound (lowest two), quasi-bound (middle), and unbound (top two) states are illustrated. The vertical shifts are commensurate with the real parts of the corresponding energy eigenvalues.

3.3. Extracting quantum impurity model parameters

One of our primary goals is extracting the coefficients of Eq. 1 from a direct simulation of a high-fidelity device model as a necessary condition for designing and operating our analog quantum coprocessor. We note that while *solving* for the properties of a quantum impurity model might be computationally difficult, determining the coefficients of Eq. 1 is more computationally straightforward. By solving for the spectrum of states in the EQI and bath using the approach described in Sections 3.1 and 3.2, we can directly extract ε_α, $t_{\alpha\beta}$, and E_m. To extract $U_{\alpha\beta\gamma\delta}$ and $V_{\alpha m}$, we require some postprocessing.

The evaluation of $U_{\alpha\beta\gamma\delta}$ can be done by using single-particle states, $\{F_\alpha(\mathbf{r})\}_\alpha$ that come out of solving Eq. 17. In particular, we make use of a trick from Ref. [57] that leverages a Poisson equation formulation. We can write $U_{\alpha\beta\gamma\delta}$ as

$$U_{\alpha\beta\gamma\delta} = \int d\mathbf{r} F_\alpha(\mathbf{r}) F_\beta(\mathbf{r}) V_{\gamma\delta}(\mathbf{r}), \text{ where} \tag{24a}$$

$$\nabla \cdot (\varepsilon \nabla V_{\gamma\delta}(\mathbf{r})) = -F_\gamma(\mathbf{r}) F_\delta(\mathbf{r}). \tag{24b}$$

We can solve Eq. 24b making use of an interior penalty discretization of the Poisson equation where

$$V_{\gamma\delta}(\mathbf{r}) \approx \sum_{e=1}^{N_e} \sum_{p=1}^{N_p(e)} d_{\gamma,\delta,e,p} g_{e,p}(\mathbf{r}), \tag{25}$$

in which we may use a different basis set from the one in Eq. 19, and the row of the resulting system of equations corresponding to $g_{e',p'}$ is

$$\sum_{e,p} d_{\gamma,\delta,e,p} \Big(\langle \nabla g_{e',p'}, \nabla g_{e,p} \rangle_{T_e} - \langle \{\{\nabla g_{e',p'}\}\}, [[g_{e,p}]] \rangle_{\partial T_e} - \langle [[g_{e',p'}]], \{\{\nabla g_{e,p}\}\} \rangle_{\partial T_e} \cdots$$
$$\cdots + \beta(T_e) \langle [[g_{e',p'}]], [[g_{e,p}]] \rangle_{\partial T_e} \Big) = \langle g_{e',p'}, F_\gamma F_\delta \rangle_{T_e}. \tag{26}$$

This sparse system of equations is formed and solved using the Generalized Minimal Residual Method (GMRES) [83] for each γ and δ. The associated integral in Eq. 24a is then evaluated for each α, β, γ, and δ by quadrature.

The extraction of $V_{\alpha m}$ requires the solution of a non-interacting scattering problem in which a particular bath mode, m, is identified and scattered off of the EQI potential. This is as simple as reformulating the eigenproblem in Eq. 17 as a scattering problem, discretizing with the interior penalty method and making use of the Hardy space method to represent the incoming and outgoing states as described in Section 3.2. In Fig. 3-2 we illustrate an exemplary calculation of the transmission probability as a function of the bath wave number for a realistic potential extracted from a model of a Ge hole device. While the transmission probabilities aren't projected onto individual EQI states to arrive at, e.g., $V_{\alpha m}$ for a specific value of α, this is itself another simple postprocessing step given the spectrum of $F_\alpha(\mathbf{r})$ from a solution to Eq. 17.

With these tools developed, we have a high-fidelity device model that can be used to design or operate an EQI system as an analog quantum simulator. In the next Section, we consider the problem of simulating experimental data that might be used to infer the Green's function as required by the self-consistency cycle described in Eq. 2.3.

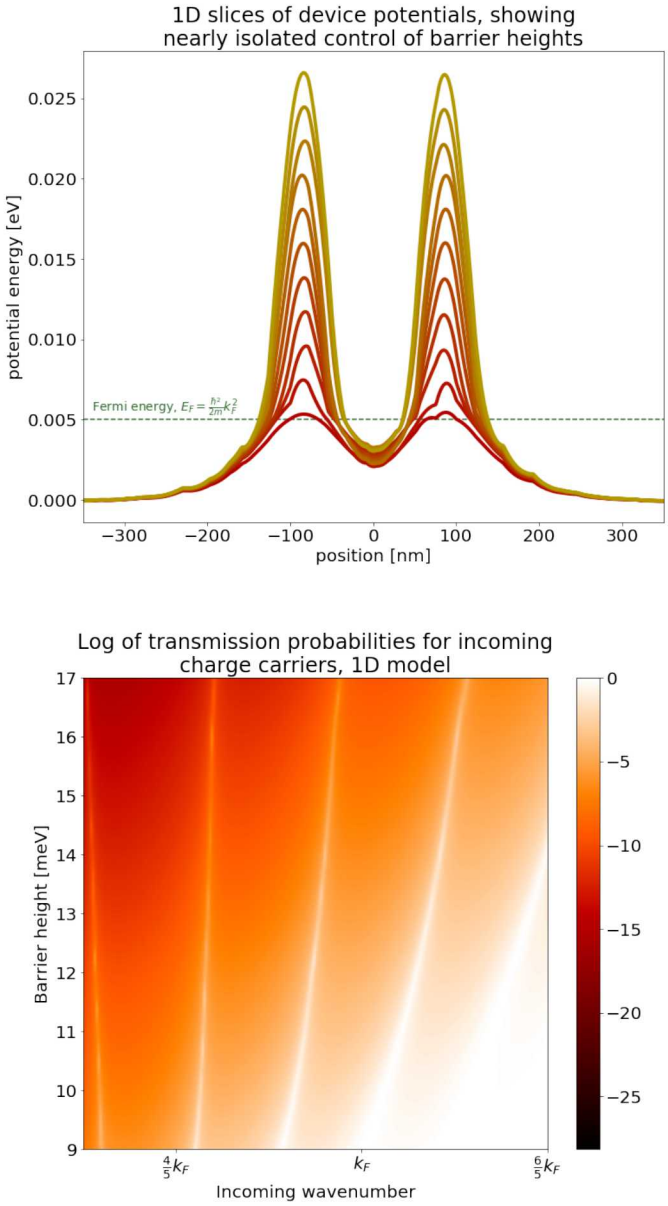

Figure 3-2 The Hardy space method used to extract the tunneling rates for a realistic dot potential for a Ge hole EQI device. (Top) A one-dimensional slice of the electrostatic potential defining the EQI. The voltages were chosen as to keep the orbital ground state and curvature of the EQI fixed while allowing the tunnel barriers between the EQI and baths to vary. (Bottom) The transmission probability through the EQI as a function of the barrier height and bath mode wavenumber for the potential on the left. Note that the transmission probability is exponentially sensitive to the barrier height and incident wave numbers, highlighting the broad tunability of the $V_{\alpha m}$ coefficients in Eq. 2c.

3.4. Simulating transport measurements

In this Section we re-derive the Meir-Wingreen formula [59] for the steady-state current through an interacting region within the biorthogonal formalism that was introduced in Section 2.1 to accommodate the use of the Hardy space method in representing incoming and outgoing particles in a bath. We first define a dual set of creation and annihilation operators, distinct from the creation and annihilation operators for fermionic states on the EQI. The relationships between these distinct sets of operators and the non-Hermitian character of operators comprised of their Hermitian analogues is then considered. We then briefly introduce the Keldysh Green's function, noting here that textbook references [67, 68] can supplement this somewhat sparse description. We are careful to point out several subtleties that arise in our biorthogonal construction, relative to the more conventional formalism. Finally, we use these definitions and tools to express the Heisenberg equation of motion for the current in a coupled EQI-bath system (i.e., an instance of Eq. 1 in which there are 2 or more baths with different chemical potentials relative to the EQI). This leads us to the Meir-Wingreen formula, which we then apply to an exemplary EQI system comprised of chains of phosphorus donors fabricated using APAM. We illustrate particular simulations that are illustrative of the types of experiments that would be needed to infer Green's functions in the context of our analog quantum coprocessor concept.

We must first define a set of creation operators $\{\hat{c}_m^\dagger\}_m$, each of which creates a fermion in state m and which anticommute,

$$\left\{\hat{c}_m^\dagger, \hat{c}_n^\dagger\right\} = 0. \tag{27}$$

This also implies that m cannot be occupied by two or more fermions. We define the action of $\hat{c}_m^\dagger$ on the vacuum state, $|0\rangle$ in the usual way,

$$\hat{c}_m^\dagger |0\rangle = |u_m\rangle, \tag{28}$$

where $|u_m\rangle$ is a single-particle basis state in which there is one fermion in u_m. Where things start to diverge from the usual approach is the need to create a second set of operators, $\{\hat{d}_m\}_m$, which also anticommute,

$$\left\{\hat{d}_m, \hat{d}_n\right\} = 0. \tag{29}$$

However, these operators create single-particle basis states that are dual to $\{|u_m\rangle\}_m$, which we will denote as $\{\langle\tilde{u}_m|\}_m$, such that

$$\langle 0|\, \hat{d}_m = \langle\tilde{u}_m|\,. \tag{30}$$

These two sets are biorthogonal,

$$\langle\tilde{u}_m|u_n\rangle = \delta_{mn}. \tag{31}$$

Typically, one would define the anticommutation relations that the creation and annihilation operators have and use this algebra to build a many-fermion Hilbert space. Here, we start with the known structure of biorthogonal basis states and work to prove that this structure is consistent with the standard anticommutation relations.

The first step is showing that the creation operators for one set will work as annihilation operators for the other set, i.e.,

$$\hat{d}_m |u_n\rangle = \delta_{mn} |0\rangle, \tag{32}$$

which can be proved by applying a biorthogonal resolution of the identity,

$$\hat{1} = |0\rangle\langle 0| + \sum_m |u_m\rangle\langle\tilde{u}_m| + \sum_{m,n\neq m} |u_m, u_n\rangle\langle\tilde{u}_m, \tilde{u}_n| + \cdots, \tag{33}$$

to the left hand side of Eq. 32. We are careful to note that the inner product between a k-particle state and an l-particle state is proportional to the delta function δ_{kl}.

We next prove that the biorthogonal sets of basis states still allow for the anticommutation relations by considering the action of such an anticommutator on the ket for the vacuum and all possible single-electron states[9],

$$\left\{\hat{c}_m^\dagger, \hat{d}_n\right\}|0\rangle = \hat{c}_m^\dagger \hat{d}_n |0\rangle + \hat{d}_n \hat{c}_m^\dagger |0\rangle \tag{34a}$$

$$= 0 + \hat{d}_n |u_m\rangle \tag{34b}$$

$$= \delta_{mn} |0\rangle, \tag{34c}$$

and

$$\left\{\hat{c}_m^\dagger, \hat{d}_n\right\}|u_o\rangle = \hat{c}_m^\dagger \hat{d}_n |u_o\rangle + \hat{d}_n \hat{c}_m^\dagger |u_o\rangle \tag{35a}$$

$$= \delta_{no}\hat{c}_m^\dagger |0\rangle + (1-\delta_{mo})\,\hat{d}_n |u_m, u_o\rangle \tag{35b}$$

$$= \delta_{no} |u_m\rangle + (1-\delta_{mo})\,\delta_{mn} |u_o\rangle + (1-\delta_{mo})\,\delta_{mo} |u_n\rangle \tag{35c}$$

$$= \delta_{mn} |u_o\rangle, \tag{35d}$$

thus

$$\left\{\hat{c}_m^\dagger, \hat{d}_n\right\} = \delta_{mn}. \tag{36}$$

We note that a physically intuitive basis for many-particle Hilbert spaces is provided by eigenstates of the number operator. The number operator for state m

$$\hat{n}_m = \hat{c}_m^\dagger \hat{d}_m, \tag{37}$$

and we are careful to note that

$$\hat{n}_m^\dagger = \left(\hat{c}_m^\dagger \hat{d}_m\right)^\dagger = \hat{d}_m^\dagger \hat{c}_m \neq \hat{n}_m. \tag{38}$$

This is an example of the fact highlighted in Section 3.2 that self-adjoint operators may no longer result in Hermitian matrices with a biorthogonal discretization.

While we may also find that $\hat{H} \neq \hat{H}^\dagger$, the form of the Schrödinger equation is not fundamentally changed by our choice of basis. Thus the time-evolution operator for a constant Hamiltonian can still be written as

$$\hat{U}(t) = e^{-i\hat{H}t}. \tag{39}$$

[9] We note that the case of multi-electron states can be handled similarly.

While this is no longer necessarily a unitary matrix the inverse can still be written as $e^{+i\hat{H}t}$. This can be used to show that the Heisenberg equation of motion of an operator $\hat{Q}$ is still[10]

$$\frac{d}{dt}\hat{Q}(t) = i\left[\hat{H}, \hat{Q}(t)\right]. \tag{40}$$

In deriving the Meir-Wingreen formula, we need to make reference to such operator evolutions on the Keldysh contour [68], denoted by $\gamma \in \mathbb{C}$. It is a contour parametrizing the argument of Heisenberg operators in real- *and* imaginary-time, and we thus substitute the $t \in \mathbb{R}$ argument of the Heisenberg operators with a $z \in \gamma$. The contour itself is directed in such a way as to define an ordering with respect to which products of Heisenberg operators are "normally ordered", thus permitting the application of Wick's theorem. Wick's theorem is used to easily construct diagrammatic perturbation theories for Green's functions and other quantities relevant to performing actual calculations. In the context of this derivation, we need it to define a contour-ordered Green's function[11]. The 1-particle Keldysh Green's function for a system with Hamiltonian $\hat{H}(z)$ is then defined by

$$iG_{mn}(z,z') = \frac{\mathrm{Tr}\left\{e^{-i\int_\gamma dz''\hat{H}(z'')}\mathcal{T}_\gamma\left[\hat{d}_m(z)\hat{c}_n^\dagger(z')\right]\right\}}{\mathrm{Tr}\left\{e^{-i\int_\gamma dz''\hat{H}(z'')}\right\}} \tag{41a}$$

$$= \delta(z,z') + \theta(z,z')\left\langle \hat{d}_m(z)\hat{c}_n^\dagger(z')\right\rangle - \theta(z',z)\left\langle \hat{c}_n^\dagger(z')\hat{d}_m(z)\right\rangle, \tag{41b}$$

where $\mathcal{T}_\gamma$ is the contour ordering operator, creation and anihilation operators are time-evolved on γ, expectation values are now taken with respect to thermal states, and $\delta(z,z')$ and $\theta(z,z')$ are defined with respect to γ.

For a non-interacting system with the quadratic Hamiltonian

$$\hat{H} = \sum_{m,n} h_{mn}\hat{c}_m^\dagger \hat{d}_n, \tag{42}$$

we derive the Heisenberg equation of motion for $G_{mn}(z,z')$ and find that it is similar to the standard case for an orthonormal basis. Differentiating with respect to z we see that

$$i\frac{d}{dz}G_{mn}(z,z') = \delta(z,z')\left\langle \hat{d}_m(z)\hat{c}_n^\dagger(z')\right\rangle + i\theta(z,z')\left\langle \left[\hat{H},\hat{d}_m(z)\right]\hat{c}_n^\dagger(z')\right\rangle \tag{43a}$$

$$- \delta(z,z')\left\langle \hat{c}_n^\dagger(z')\hat{d}_m(z)\right\rangle - i\theta(z,z')\left\langle \hat{c}_n^\dagger(z')\left[\hat{H},\hat{d}_m(z)\right]\right\rangle \tag{43b}$$

$$= \delta(z,z')\delta_{mn} + \sum_o h_{mo}G_{on}(z,z'), \tag{43c}$$

where we note that we have chosen a quadratic Hamiltonian to prevent a hierarchy of dependencies on n-particle Green's functions as was discussed in Section 2.2. Suppressing the dependence on a specific single-particle basis this can be rewritten as

$$\left(i\frac{d}{dz} - \hat{h}\right)\hat{G}(z,z') = \delta(z,z')\hat{1}, \tag{44}$$

[10] We first encountered the Heisenberg equation of motion in Eq. 6.

[11] In contrast to the time-ordered Green's function in Eq. 7.

where $\hat{h}$ denotes the projection of $\hat{H}$ onto a single-particle Hilbert space, rather than the full Fock space.

We can solve Eq. 44 in the Fourier domain if we assume that our system will reach a steady state, in which case $\hat{G}(z,z') \to \hat{G}(z-z')$ and

$$\hat{G}(\omega) = \left[\omega\hat{1} - \hat{h}\right]^{-1}. \tag{45}$$

As with the time-ordered Green's functions in Section 2, we can define retarded and advanced components of this Green's function. The retarded Green's function corresponds to $z < z'$ and is given in the Fourier domain as

$$\hat{G}^R(\omega) = \lim_{\eta\to 0^+} \left[(\omega + i\eta)\hat{1} - \hat{h}\right]^{-1}, \tag{46}$$

and the advanced Green's function corresponds to $z > z'$, given by

$$\hat{G}^A(\omega) = \lim_{\eta\to 0^+} \left[(\omega - i\eta)\hat{1} - \hat{h}\right]^{-1}. \tag{47}$$

We also introduce lesser and greater Green's functions that are defined in the time domain as

$$G^<_{mn}(z,z') = -i\left\langle \hat{c}^\dagger_n(z')\hat{d}_m(z)\right\rangle \tag{48}$$

and

$$G^>_{mn}(z,z') = -i\left\langle \hat{d}_m(z)\hat{c}^\dagger_n(z')\right\rangle. \tag{49}$$

These latter two Green's functions will appear in the Meir-Wingreen formula and it is useful to first see their relationship to the retarded and advanced Green's functions through the fluctuation-dissipation theorem.

Differentiating Eq. 48 with respect to the time arguments and solving relative to initial conditions at $(z,z') \to (0,0)$, we see that

$$\hat{G}^<(z,z') = e^{+i\hat{h}z}\hat{G}^<(0,0)e^{-i\hat{h}z'}. \tag{50}$$

Restoring the dependence on an explicit single-particle basis it should be clear that

$$G^<_{mn}(0,0) = -i\left\langle \hat{c}^\dagger_n(0)\hat{d}_m(0)\right\rangle = -i\delta_{mn}\left\langle \hat{c}^\dagger_m\hat{d}_m\right\rangle, \tag{51}$$

which is simply the particle number in orbital m in the initial state. As we are starting in a thermal state, this is simply a Fermi-Dirac distribution. We can then Fourier transform Eq. 50 to arrive at

$$\begin{aligned}
\hat{G}^<(\omega) &= -f(\omega)\,\delta\left(\omega\hat{1} - \hat{h}\right) && \text{(52a)}\\
&= -f(\omega)\lim_{\eta\to 0^+}\left(\left[(\omega+i\eta)\hat{1} - \hat{h}\right]^{-1} - \left[(\omega-i\eta)\hat{1} - \hat{h}\right]^{-1}\right) && \text{(52b)}\\
&= -f(\omega)\left(\hat{G}^R(\omega) - \hat{G}^A(\omega)\right) && \text{(52c)}
\end{aligned}$$

where f is the Fermi-Dirac distribution. This is the fluctuation-dissipation theorem. A similar equation including the complement of the Fermi-Dirac distribution can be derived for $\hat{G}^{>}$. We were careful to have shown these relationships because they imply that the retarded and advanced Green's functions are related by

$$\hat{G}^A(\omega) = \left(\hat{G}^R(\omega)^{-1} - 2i\eta\hat{1}\right)^{-1} \neq \hat{G}^R(\omega)^\dagger. \tag{53}$$

Whereas the retarded and advanced Green's functions would be related through Hermitian conjugation in the usual case for an orthogonal system, for our biorthogonal case this relationship is more subtle.

We now have the definitions and tools necessary to derive the Meir-Wingreen formula for current through an interacting system. We will continue to use $\hat{c}_m^\dagger$ and $\hat{d}_m$ to denote the creation and annihilation operators for bath modes that are being injected into the system through a bias. As before, we will use $\hat{a}_\alpha^\dagger$ and $\hat{a}_\alpha$ as the creation and annihilation operators on the impurity. Note that because an orthonormal basis is a special case of a biorthogonal basis where the left and right basis sets are the same, all of the Green's function relationships that we have demonstrated apply to the impurity, as well. This also suggests that the derivation of the formula for the current is relatively similar to the standard orthonormal case.

We consider a Hamiltonian of the form in Eq. 1, repeated for clarity,

$$\hat{H} = \hat{H}_i + \hat{H}_b + \hat{H}_{i-b}, \tag{54}$$

where $\hat{H}_i$ is the same as in Section 2, $\hat{H}_b$ is the total energy of the states in the leads, and we update $\hat{H}_{i-b}$ to reflect the new biorthogonal operator algebra,

$$\hat{H}_{i-b} = \sum_{m,\alpha}\left(V_{m\alpha}\hat{c}_m^\dagger\hat{a}_\alpha + V_{\alpha m}\hat{a}_\alpha^\dagger\hat{d}_m\right), \tag{55}$$

then we can examine the Heisenberg evolution of the total number operator for the bath,

$$\hat{N}_b = \sum_m \hat{c}_m^\dagger\hat{d}_m, \tag{56}$$

to get the current flowing out of the associated lead. If $\hat{H}_b$ conserves the electron number in the bath, we find that

$$\left[\hat{H}, \hat{c}_k^\dagger\hat{d}_k\right] = \left[\hat{H}_{i-b}, \hat{c}_k^\dagger\hat{d}_k\right] = -\sum_{j,\alpha}\delta_{jk}\left(V_{j\alpha}\hat{c}_k^\dagger\hat{a}_\alpha - V_{\alpha j}\hat{a}_\alpha^\dagger\hat{d}_k\right). \tag{57}$$

Because the current flowing from the lead is the time derivative of the expectation value of the number of fermions in the bath, we can use the above expression with the Heisenberg equation of motion to determine an expression for the current at time z as

$$\begin{aligned}
I_b(z) &= \frac{d}{dz}\left\langle\hat{N}_b(z)\right\rangle && \text{(58a)}\\
&= i\sum_k\left\langle\left[\hat{H}, \hat{c}_k^\dagger(z)\hat{d}_k(z)\right]\right\rangle && \text{(58b)}\\
&= -i\sum_{j,\alpha}\sum_k\delta_{jk}\left(V_{j\alpha}\left\langle\hat{c}_k^\dagger(z)\hat{a}_\alpha(z)\right\rangle - V_{\alpha j}\left\langle\hat{a}_\alpha^\dagger(z)\hat{d}_k(z)\right\rangle\right) && \text{(58c)}\\
&= \mathrm{Tr}\left\{\hat{h}_{i-b}\hat{G}^<_{b-i}(z,z) - \hat{h}_{b-i}\hat{G}^<_{i-b}(z,z)\right\}, && \text{(58d)}
\end{aligned}$$

where $\hat{h}_{b-i}$ and $\hat{h}_{i-b}$ are the single-particle matrix defined by the coefficients in $\hat{H}_{i-b}$, going from the bath to the impurity and the vice versa, respectively. We have also introduced projections of the time domain lesser Green's functions $\hat{G}^<_{b-i}(z,z)$ and $\hat{G}^<_{i-b}(z,z)$ with the same convention.

We will next use Eq. 58d to derive the expression for the steady-state current. We begin by noting that $\hat{G}^<_{Li}(t,t) \neq -\hat{G}^<_{iL}(t,t)^\dagger$, in contrast with the standard case using an orthonormal basis, preventing us from simplifying this equation in the usual textbook fashion [68]. In order to develop a new expression for this quantity, we begin with the Keldysh Green's function for the composite system of the bath and the impurity, split into parts. Assuming no interactions on the impurity for simplicity[12], we can write the equation of motion as

$$\left(i\frac{d}{dz} - \begin{bmatrix} \hat{h}_b & \hat{h}_{b-i} \\ \hat{h}_{i-b} & \hat{h}_i \end{bmatrix}\right) \begin{bmatrix} \hat{G}_b(z,z') & \hat{G}_{b-i}(z,z') \\ \hat{G}_{i-b}(z,z') & \hat{G}_i(z,z') \end{bmatrix} = \delta(z,z')\hat{1}, \tag{59}$$

where $\hat{h}_{b/i}$ is the single-particle Hamiltonian on the bath/impurity and $\hat{G}_{b/i}(z,z')$ is the corresponding Keldysh Green's function. Elimination can be used to define the Green's function on the impurity as

$$\left(i\frac{d}{dz} - \hat{h}_i\right)\hat{G}_i = \delta(z,z')\hat{1} + \hat{h}_{i-b}\hat{G}_{b-i}(z,z'), \tag{60}$$

and we can formally solve this equation by defining $\hat{G}_{b-i}$ to be

$$\hat{G}_{b-i}(z,z') = \int_\gamma dz''\, \hat{g}_b(z,z'')\hat{h}_{b-i}\hat{G}_i(z'',z), \tag{61}$$

where $\hat{g}_b(z,z')$ is the Green's function of the bath decoupled from the impurity. Defining $\hat{G}_{b-i}(z,z')$ as an integral over the Keldysh contour like this allows us to use Langreth rules to express the lesser Green's function [68]. Defining the embedding self-energy of the bath as

$$\hat{\Sigma}_b(z,z') = \hat{h}_{i-b}\hat{g}_b(z,z')\hat{h}_{b-i}, \tag{62}$$

we can rewrite the first term on the right-hand side of Eq. 58d in the steady state as

$$\hat{h}_{i-b}\hat{G}^<_{b-i}(z,z) = \int dz' \left(\hat{\Sigma}^<_b(z,z')\hat{G}^A_i(z',z) + \hat{\Sigma}^R_b(z,z')\hat{G}^<_i(z',z)\right) \tag{63a}$$

$$= \frac{1}{2\pi}\int d\omega \left(\hat{\Sigma}^<_b(\omega)\hat{G}^A_i(\omega) + \hat{\Sigma}^R_b(\omega)\hat{G}^<_i(\omega)\right). \tag{63b}$$

Similar substitutions can be made for $\hat{h}_{b-i}\hat{G}^<_{i-b}(z,z)$, and with that we finally arrive at the Meir-Wingreen formula for the current in steady state,

$$I_b = \frac{1}{2\pi}\int d\omega \,\mathrm{Tr}\left\{\hat{\Sigma}^<_b(\omega)\hat{G}^A_i(\omega) + \hat{\Sigma}^R_b(\omega)\hat{G}^<_i(\omega) - \hat{\Sigma}^<_i(\omega)\hat{G}^A_b(\omega) - \hat{\Sigma}^R_i(\omega)\hat{G}^<_b(\omega)\right\}, \tag{64}$$

where $\hat{\Sigma}_i$ is the embedding of the impurity to the lead defined similarly to the equation for $\hat{\Sigma}_b$. Note that the Green's functions for the bath and impurity are linked, as Eq. 60 implies. A change to the lesser Green's function for the impurity, for example, affects all the other Green's functions

[12] These would be absorbed into appropriate self-energies in a more complete derivation.

involved here. Luckily, Eqs. 52 and 53 imply that for steady state systems with no interactions, the ability to calculate the retarded component of the Green's function allows one to calculate all other components of the Green's function. This and Eq. 60 transformed to the frequency domain,

$$\hat{G}_i(\omega) = \left[\omega\hat{1} - \hat{h}_i - \hat{\Sigma}_b(\omega)\right]^{-1}, \tag{65}$$

give us all of the tools we need to calculate a current through an interacting region.

We have implemented this approach to computing the current through interacting regions for Hamiltonians of the form in Eq. 1, noting that we are principally concerned with EQIs in contact with 2 or more baths and that this generalization is straightforward. As a benchmark problem, we study two EQIs comprised of phosphorus donor chains coupled to 2 baths in Fig. 3-3 We use the formulation of multi-valley effective mass theory considered in Ref. [62] to generate Hamiltonian coefficients for EQIs consisting of both 2- and 5-donor chain. In the results that we have shown, we chose the bias windows for the baths relative to the EQIs such that we can see Coulomb blockade, i.e., regions in which the current through the chain is suppressed due to the prohibitive energetic cost associated with having too many electrons on the EQI. In bias spectroscopy experiments, one typically looks at the voltage derivative of this signal (i.e., the differential conductance) which is computed and illustrated in Fig. 3-4. In this example the regions of high differential conductivity correspond to many-particle eigenstates of the EQI being brought into the bias window of the device.

These calculations simulate precisely the sort of experiment that we would like to use to infer Green's functions for EQIs in the context of our analog quantum coprocessor concept. It is evident from the form of Eq. 64 that its voltage derivative provides us with access to spectrally-resolved information about $\hat{G}_i$, provided a model for $\hat{G}_b$, $\hat{\Sigma}_b$, $\hat{\Sigma}_i$. Thus we can imagine bias spectroscopy experiments with a 3-terminal device, in which 2 are used to supply a probe current and the 3rd is used to serve as the controllably coupled bath in our single impurity model. The differential conductance as measured by the 2 terminals used to supply the current can then be used to infer $\hat{G}_i$ at real frequencies which can be Hilbert transformed to yield the Green's function at the Matsubara frequencies needed to ensure self-consistency with respect to a target lattice problem, as described in Section 2.3. One can also imagine a less intrusive measurement that makes use of a 1-terminal device with an adjacent charge sensor, in which the spectrum of current fluctuations in the charge sensor can be used to infer $\hat{G}_i$ in real-time, starting from Eq. 58d. At the close of our project the relative advantages and disadvantages of these two approaches remain a topic of ongoing research.

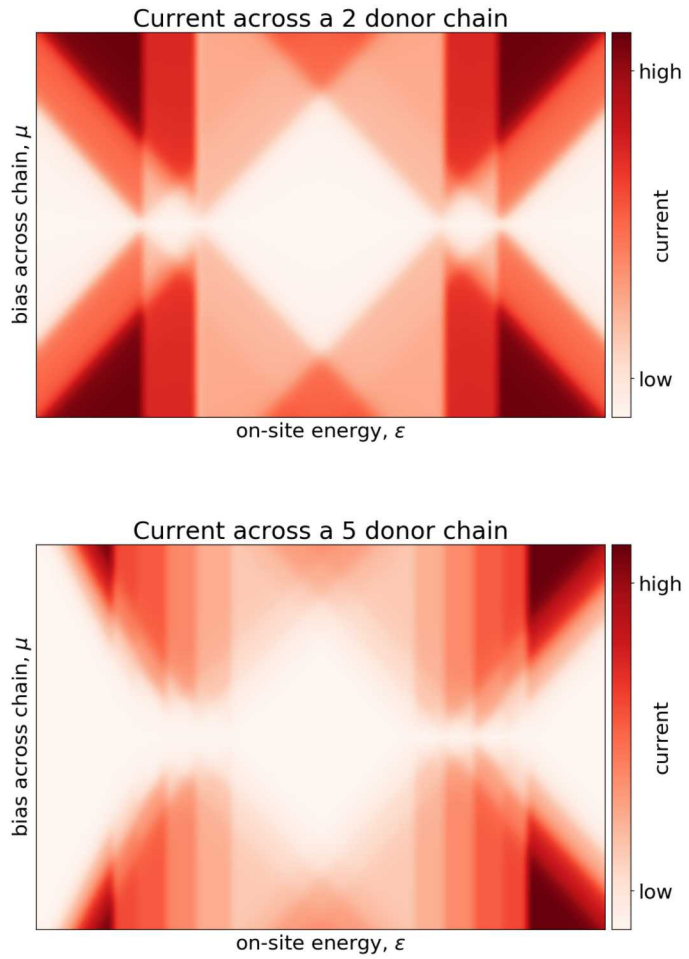

Figure 3-3 Exemplary calculations of the current across two APAM-fabricated chains. (Top) Current through a chain of 2 single-donor EQIs. (Bottom) Current through a chain of 5 single-donor EQIs. In both cases, the vertical axis corresponds to a source-drain bias voltage from one end of the chain to the other and the horizontal axis corresponds to the uniform on-site energy of each EQI controlled using, e.g., a top-gate [2]. The regions of low current correspond to Coulomb blockade of transport through the chain.

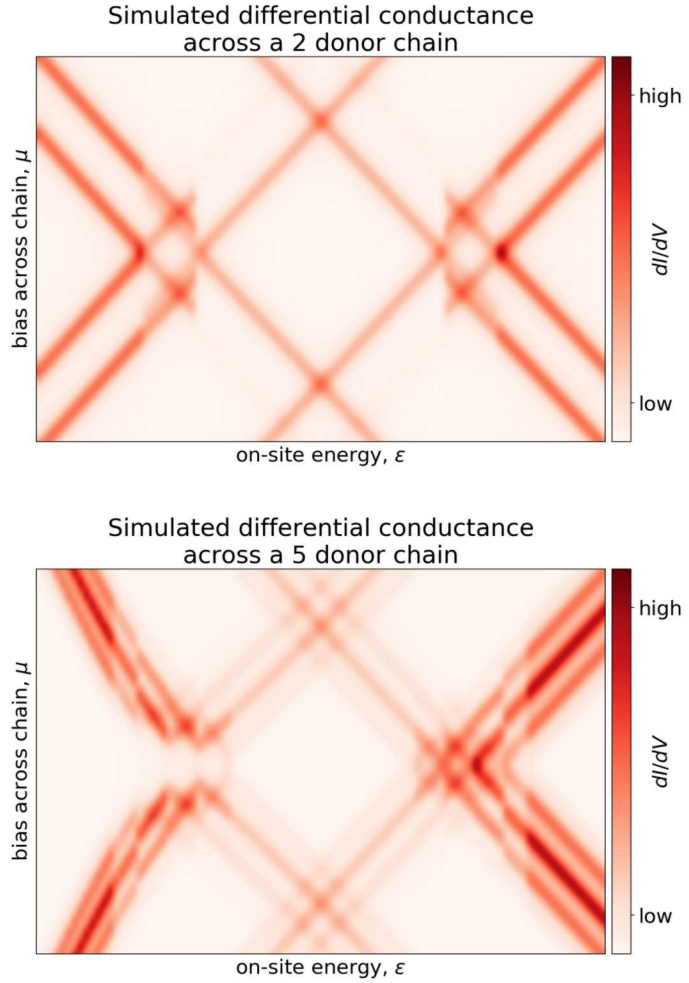

Figure 3-4 Exemplary calculations of the differential conductance across two APAM-fabricated chains. (Top) Differential conductance across a chain of 2 single-donor EQIs. (Bottom) Differential conducatance across a chain of 5 single-donor EQIs. In both cases, the vertical axis corresponds to a source-drain bias voltage from one end of the chain to the other and the horizontal axis corresponds to the uniform on-site energy of each EQI controlled using, e.g., a top-gate [2]. The charge transitions corresponding to high values of the differential conductance correspond to eigenstates of the chains being brought into the bias window, giving us a direct map of the energy-level structure of the two chains.

4. CONCLUSION

The approach and tools developed in this report are the foundation for realizing our analog quantum coprocessor concept in practice. The most obvious next step is to build a single EQI system connected to a single tunable bath in an attempt to realize two-site DMFT [51]. While this particular instance of DMFT is far from computationally intractable, it is a simple exemplary case that 1) captures phenomenology relevant to strongly correlated systems and 2) is analytically tractable in such a way that our approach can be verified and validated.

As for the particular material system that should be targeted, our recommendation is to pursue Si electron-based quantum dot devices, Ge hole-based quantum dot devices, and APAM-fabricated dopant devices due to local expertise. All of these systems have rich physics beyond the simple isotropic effective mass theory described in Section 2.1. Fortunately, progress over the course of this LDRD has also augmented our ability to study these systems, namely a Luttinger-Kohn-based approach to studying the Ge hole devices and anisotropic atomic orbitals for dopant devices. This capability will have impacts beyond the scope of the particular application to designing and operating the analog quantum coprocessor concept described in this report.

There are a few other future prospects worth mentioning. We note that the DMFT mapping on which this approach is based is only exact in the infinite-dimensional limit. This means that the particular embedding that we're studying is an approximation in dimensions corresponding to physical systems (e.g., two or three). Nevertheless, one can replace the single impurity model with increasingly large clusters to mitigate the error due to this approximation. We note that creating increasingly large and structured EQIs is one of the dimensions along which we might imagine scaling our approach. We also note that *driven* impurity models might be an opportunity for an analog quantum simulation platform based on EQIs. In particular, we note Ref. [84] which studies the computational complexity of the periodically-driven Anderson impurity model and illustrates the rapid growth in the EQI-bath entanglement entropy in a certain regime of driving. While this entropy is itself predicated on the specific ordering of the bath modes, the fact that it continues to grow rapidly even with a particularly optimal ordering is suggestive of the fact that this is also a hard problem. The tools developed in this LDRD could also be used to design an EQI-based simulator for this model, as well.

REFERENCES

[1] B. Bauer, D. Wecker, A. J. Millis, M. B. Hastings, and M. Troyer. Hybrid quantum-classical approach to correlated materials. *Physical Review X*, 6(3):031045, 2016.

[2] E. M. Anderson, D. M. Campbell, L. Maurer, A. Baczewski, M. T. Marshall, T. Lu, P. Lu, L. Tracy, S. W. Schmucker, D. R. Ward, et al. Low thermal budget high-k/metal surface gate for buried donor-based devices. *Journal of Physics: Materials*, 2020.

[3] R. P. Feynman. Simulating physics with computers. *Int. J. Theor. Phys*, 21(6/7), 1982.

[4] P. A. M. Dirac. Quantum mechanics of many-electron systems. *Proceedings of the Royal Society of London. Series A, Containing Papers of a Mathematical and Physical Character*, 123(792):714–733, 1929.

[5] S. Lloyd. Universal quantum simulators. *Science*, pages 1073–1078, 1996.

[6] D. S. Abrams and S. Lloyd. Simulation of many-body Fermi systems on a universal quantum computer. *Physical Review Letters*, 79(13):2586, 1997.

[7] D. S. Abrams and S. Lloyd. Quantum algorithm providing exponential speed increase for finding eigenvalues and eigenvectors. *Physical Review Letters*, 83(24):5162, 1999.

[8] A. Aspuru-Guzik, A. D. Dutoi, P. J. Love, and M. Head-Gordon. Simulated quantum computation of molecular energies. *Science*, 309(5741):1704–1707, 2005.

[9] S. P. Jordan, K. S. Lee, and J. Preskill. Quantum algorithms for quantum field theories. *Science*, 336(6085):1130–1133, 2012.

[10] A. Russo, K. Rudinger, B. Morrison, and A. Baczewski. Evaluating energy differences on a quantum computer with robust phase estimation. *arXiv preprint arXiv:2007.08697*, 2020.

[11] A. Y. Kitaev. Quantum measurements and the Abelian stabilizer problem. *arXiv preprint quant-ph/9511026*, 1995.

[12] M. A. Nielsen and I. Chuang. Quantum computation and quantum information, 2002.

[13] J. Hubbard. Electron correlations in narrow energy bands. *Proceedings of the Royal Society of London. Series A. Mathematical and Physical Sciences*, 276(1365):238–257, 1963.

[14] J. LeBlanc, A. E. Antipov, F. Becca, I. W. Bulik, G. K.-L. Chan, C.-M. Chung, Y. Deng, M. Ferrero, T. M. Henderson, C. A. Jiménez-Hoyos, et al. Solutions of the two-dimensional Hubbard model: benchmarks and results from a wide range of numerical algorithms. *Physical Review X*, 5(4):041041, 2015.

[15] R. Babbush, C. Gidney, D. W. Berry, N. Wiebe, J. McClean, A. Paler, A. Fowler, and H. Neven. Encoding electronic spectra in quantum circuits with linear T complexity. *Physical Review X*, 8(4):041015, 2018.

[16] G. A. Quantum et al. Hartree-fock on a superconducting qubit quantum computer. *Science*, 369(6507):1084–1089, 2020.

[17] L. H. Thomas. The calculation of atomic fields. In *Mathematical Proceedings of the Cambridge Philosophical Society*, volume 23, pages 542–548. Cambridge University Press, 1927.

[18] E. Fermi. Un metodo statistico per la determinazione di alcune priorieta dell'atome. *Rend. Accad. Naz. Lincei*, 6(602-607):32, 1927.

[19] D. Hartree. The Wave Mechanics of an Atom with a Non-Coulomb Central Field. Part I. Theory and Methods. In *Mathematical Proceedings of the Cambridge Philosophical Society*, volume 24, pages 89–110. Cambridge University Press, 1928.

[20] J. C. Slater. The self consistent field and the structure of atoms. *Physical Review*, 32(3):339, 1928.

[21] V. Fock. Näherungsmethode zur Lösung des quantenmechanischen Mehrkörperproblems. *Zeitschrift für Physik*, 61(1-2):126–148, 1930.

[22] A. Pribram-Jones, D. A. Gross, and K. Burke. DFT: A theory full of holes? *Annual review of physical chemistry*, 66:283–304, 2015.

[23] R. J. Bartlett and M. Musiał. Coupled-cluster theory in quantum chemistry. *Reviews of Modern Physics*, 79(1):291, 2007.

[24] W. Foulkes, L. Mitas, R. Needs, and G. Rajagopal. Quantum Monte Carlo simulations of solids. *Reviews of Modern Physics*, 73(1):33, 2001.

[25] P. Wocjan and S. Zhang. Several natural BQP-Complete problems. *arXiv preprint quant-ph/0606179*, 2006.

[26] T. Proctor, K. Rudinger, K. Young, E. Nielsen, and R. Blume-Kohout. Measuring the Capabilities of Quantum Computers. *arXiv preprint arXiv:2008.11294*, 2020.

[27] S. Somaroo, C. Tseng, T. Havel, R. Laflamme, and D. G. Cory. Quantum simulations on a quantum computer. *Physical review letters*, 82(26):5381, 1999.

[28] E. Manousakis. A quantum-dot array as model for copper-oxide superconductors: A dedicated quantum simulator for the many-fermion problem. *Journal of low temperature physics*, 126(5-6):1501–1513, 2002.

[29] D. Porras and J. I. Cirac. Effective quantum spin systems with trapped ions. *Physical review letters*, 92(20):207901, 2004.

[30] I. M. Georgescu, S. Ashhab, and F. Nori. Quantum simulation. *Reviews of Modern Physics*, 86(1):153, 2014.

[31] S. Misra, D. R. Ward, A. D. Baczewski, Q. Campbell, S. W. Schmucker, A. Mounce, L. A. Tracy, T.-M. Lu, M. T. Marshall, and D. M. Campbell. Designer quantum materials. Technical report, Sandia National Lab.(SNL-NM), Albuquerque, NM (United States), 2019.

[32] M. E. Fisher. The renormalization group in the theory of critical behavior. *Reviews of Modern Physics*, 46(4):597, 1974.

[33] K. G. Wilson. The renormalization group: Critical phenomena and the Kondo problem. *Reviews of modern physics*, 47(4):773, 1975.

[34] M. Sarovar, J. Zhang, and L. Zeng. Reliability of analog quantum simulation. *EPJ quantum technology*, 4(1):1, 2017.

[35] P. M. Poggi, N. K. Lysne, K. W. Kuper, I. H. Deutsch, and P. S. Jessen. Quantifying the sensitivity to errors in analog quantum simulation. *arXiv preprint arXiv:2007.01901*, 2020.

[36] D. R. Ward, S. W. Schmucker, E. M. Anderson, E. Bussmann, L. Tracy, T.-M. Lu, L. N. Maurer, A. Baczewski, D. M. Campbell, M. T. Marshall, and S. Misra. Atomic precision advanced manufacturing for digital electronics. *Electronic Device Failure Analysis*, 22(1): 4–11, 2020.

[37] F. Borjans, X. Croot, X. Mi, M. Gullans, and J. Petta. Resonant microwave-mediated interactions between distant electron spins. *Nature*, 577(7789):195–198, 2020.

[38] Y. He, S. Gorman, D. Keith, L. Kranz, J. Keizer, and M. Simmons. A two-qubit gate between phosphorus donor electrons in silicon. *Nature*, 571(7765):371–375, 2019.

[39] N. Hendrickx, D. Franke, A. Sammak, G. Scappucci, and M. Veldhorst. Fast two-qubit logic with holes in germanium. *Nature*, 577(7791):487–491, 2020.

[40] R. M. Jock, N. T. Jacobson, P. Harvey-Collard, A. M. Mounce, V. Srinivasa, D. R. Ward, J. Anderson, R. Manginell, J. R. Wendt, M. Rudolph, et al. A silicon metal-oxide-semiconductor electron spin-orbit qubit. *Nature communications*, 9(1):1–8, 2018.

[41] C. H. Yang, R. Leon, J. Hwang, A. Saraiva, T. Tanttu, W. Huang, J. C. Lemyre, K. W. Chan, K. Tan, F. E. Hudson, et al. Operation of a silicon quantum processor unit cell above one Kelvin. *Nature*, 580(7803):350–354, 2020.

[42] S. Sasaki, S. De Franceschi, J. Elzerman, W. Van der Wiel, M. Eto, S. Tarucha, and L. Kouwenhoven. Kondo effect in an integer-spin quantum dot. *Nature*, 405(6788): 764–767, 2000.

[43] W. Van der Wiel, S. De Franceschi, T. Fujisawa, J. Elzerman, S. Tarucha, and L. Kouwenhoven. The Kondo effect in the unitary limit. *Science*, 289(5487):2105–2108, 2000.

[44] L. Kouwenhoven and L. Glazman. Revival of the Kondo effect. *Physics world*, 14(1):33, 2001.

[45] A. Georges and G. Kotliar. Hubbard model in infinite dimensions. *Physical Review B*, 45 (12):6479, 1992.

[46] A. Georges, G. Kotliar, W. Krauth, and M. J. Rozenberg. Dynamical mean-field theory of strongly correlated fermion systems and the limit of infinite dimensions. *Reviews of Modern Physics*, 68(1):13, 1996.

[47] G. Kotliar, S. Y. Savrasov, K. Haule, V. S. Oudovenko, O. Parcollet, and C. Marianetti. Electronic structure calculations with dynamical mean-field theory. *Reviews of Modern Physics*, 78(3):865, 2006.

[48] M. Caffarel and W. Krauth. Exact diagonalization approach to correlated fermions in infinite dimensions: Mott transition and superconductivity. *Physical review letters*, 72(10):1545, 1994.

[49] E. Gull, A. J. Millis, A. I. Lichtenstein, A. N. Rubtsov, M. Troyer, and P. Werner. Continuous-time Monte Carlo methods for quantum impurity models. *Reviews of Modern Physics*, 83(2):349, 2011.

[50] T. Zhu, C. A. Jiménez-Hoyos, J. McClain, T. C. Berkelbach, and G. K.-L. Chan. Coupled-cluster impurity solvers for dynamical mean-field theory. *Physical Review B*, 100 (11):115154, 2019.

[51] M. Potthoff. Two-site dynamical mean-field theory. *Physical Review B*, 64(16):165114, 2001.

[52] J. M. Kreula, L. García-Álvarez, L. Lamata, S. R. Clark, E. Solano, and D. Jaksch. Few-qubit quantum-classical simulation of strongly correlated lattice fermions. *EPJ Quantum Technology*, 3(1):1–19, 2016.

[53] T. Keen, T. Maier, S. Johnston, and P. Lougovski. Quantum-classical simulation of two-site dynamical mean-field theory on noisy quantum hardware. *Quantum Science and Technology*, 5(3):035001, 2020.

[54] B. Jaderberg, A. Agarwal, K. Leonhardt, M. Kiffner, and D. Jaksch. Minimum Hardware Requirements for Hybrid Quantum-Classical DMFT. *arXiv preprint arXiv:2002.04612*, 2020.

[55] I. Rungger, N. Fitzpatrick, H. Chen, C. Alderete, H. Apel, A. Cowtan, A. Patterson, D. M. Ramo, Y. Zhu, N. H. Nguyen, et al. Dynamical mean field theory algorithm and experiment on quantum computers. *arXiv preprint arXiv:1910.04735*, 2019.

[56] S. Bravyi and D. Gosset. Complexity of quantum impurity problems. *Communications in Mathematical Physics*, 356(2):451–500, 2017.

[57] J. K. Gamble, E. Nielsen, A. D. Baczewski, J. E. Moussa, X. Gao, A. G. Salinger, and R. P. Muller. *Advanced Electronic Structure Calculations for Nanoelectronics*. Springer, 2020.

[58] T. Hohage and L. Nannen. Hardy space infinite elements for scattering and resonance problems. *SIAM journal on numerical analysis*, 47(2):972–996, 2009.

[59] Y. Meir and N. S. Wingreen. Landauer formula for the current through an interacting electron region. *Physical review letters*, 68(16):2512, 1992.

[60] X. Gao, E. Nielsen, R. P. Muller, R. W. Young, A. G. Salinger, N. C. Bishop, M. P. Lilly, and M. S. Carroll. Quantum computer aided design simulation and optimization of semiconductor quantum dots. *Journal of Applied Physics*, 114(16):164302, 2013.

[61] S. Asaad, V. Mourik, B. Joecker, M. A. Johnson, A. D. Baczewski, H. R. Firgau, M. T. Mądzik, V. Schmitt, J. J. Pla, F. E. Hudson, et al. Coherent electrical control of a single high-spin nucleus in silicon. *Nature*, 579(7798):205–209, 2020.

[62] J. K. Gamble, N. T. Jacobson, E. Nielsen, A. D. Baczewski, J. E. Moussa, I. Montaño, and R. P. Muller. Multivalley effective mass theory simulation of donors in silicon. *Physical Review B*, 91(23):235318, 2015.

[63] J. K. Gamble, P. Harvey-Collard, N. T. Jacobson, A. D. Baczewski, E. Nielsen, L. Maurer, I. Montaño, M. Rudolph, M. Carroll, C. Yang, et al. Valley splitting of single-electron si mos quantum dots. *Applied Physics Letters*, 109(25):253101, 2016.

[64] A. Y. Kitaev, A. Shen, and M. Vyalyi. *Classical and Quantum Computation*. American Mathematical Society, 2002.

[65] X. Gao, E. Nielsen, R. P. Muller, R. Young, A. Salinger, N. Bishop, and M. Carroll. The QCAD framework for quantum device modeling. In *2012 15th International Workshop on Computational Electronics*, pages 1–4. IEEE, 2012.

[66] A. L. Fetter and J. D. Walecka. *Quantum Theory of Many-particle Systems*. Courier Corporation, 2003.

[67] A. Kamenev. *Field Theory of Non-Equilibrium Systems*. Cambridge University Press, 2011.

[68] G. Stefanucci and R. Van Leeuwen. *Nonequilibrium Many-Body Theory of Quantum Systems: A Modern Introduction*. Cambridge University Press, 2013.

[69] F. W. Byron and R. W. Fuller. *Mathematics of Classical and Quantum Physics*, volume 1. Courier Corporation, 1992.

[70] J. Sakurai et al. Modern quantum mechanics, 1994.

[71] COMSOL AB, Stockholm, Sweden. COMSOL Multiphysics® v. 5.4. URL https://www.comsol.com.

[72] J. Douglas and T. Dupont. Interior penalty procedures for elliptic and parabolic galerkin methods. In *Computing methods in applied sciences*, pages 207–216. Springer, 1976.

[73] D. N. Arnold. An interior penalty finite element method with discontinuous elements. *SIAM journal on numerical analysis*, 19(4):742–760, 1982.

[74] J. S. Hesthaven and T. Warburton. *Nodal discontinuous Galerkin methods: algorithms, analysis, and applications*. Springer Science & Business Media, 2007.

[75] L. Lin, J. Lu, L. Ying, and E. Weinan. Adaptive local basis set for Kohn–Sham density functional theory in a discontinuous Galerkin framework I: Total energy calculation. *Journal of Computational Physics*, 231(4):2140–2154, 2012.

[76] A. V. Knyazev. Toward the optimal preconditioned eigensolver: Locally optimal block preconditioned conjugate gradient method. *SIAM journal on scientific computing*, 23(2): 517–541, 2001.

[77] D. Ruprecht, A. Schädle, F. Schmidt, and L. Zschiedrich. Transparent boundary conditions for time-dependent problems. *SIAM Journal on Scientific Computing*, 30(5):2358–2385, 2008.

[78] L. Nannen and A. Schädle. Hardy space infinite elements for Helmholtz-type problems with unbounded inhomogeneities. *Wave Motion*, 48(2):116–129, 2011.

[79] L. Nannen, T. Hohage, A. Schädle, and J. Schöberl. Exact sequences of high order Hardy space infinite elements for exterior Maxwell problems. *SIAM Journal on Scientific Computing*, 35(2):A1024–A1048, 2013.

[80] T. Hohage and L. Nannen. Convergence of infinite element methods for scalar waveguide problems. *BIT Numerical Mathematics*, 55(1):215–254, 2015.

[81] M. Halla, T. Hohage, L. Nannen, and J. Schöberl. Hardy space infinite elements for time harmonic wave equations with phase and group velocities of different signs. *Numerische Mathematik*, 133(1):103–139, 2016.

[82] S. Kramer. Finite-element methods for spatially resolved mesoscopic electron transport. *Physical Review B*, 88(12):125308, 2013.

[83] Y. Saad and M. H. Schultz. Gmres: A generalized minimal residual algorithm for solving nonsymmetric linear systems. *SIAM Journal on scientific and statistical computing*, 7(3): 856–869, 1986.

[84] Z. He and A. J. Millis. Entanglement entropy and computational complexity of the periodically driven anderson impurity model. *Physical Review B*, 99(20):205138, 2019.

[85] X. Gao, D. Mamaluy, E. Nielsen, R. W. Young, A. Shirkhorshidian, M. P. Lilly, N. C. Bishop, M. S. Carroll, and R. P. Muller. Efficient self-consistent quantum transport simulator for quantum devices. *Journal of Applied Physics*, 115(13):133707, 2014.

[86] F. Arute, K. Arya, R. Babbush, D. Bacon, J. C. Bardin, R. Barends, S. Boixo, M. Broughton, B. B. Buckley, D. A. Buell, et al. Hartree-Fock on a superconducting qubit quantum computer. *arXiv preprint arXiv:2004.04174*, 2020.

APPENDIX A. ANISOTROPIC ATOMIC ORBITALS

We begin by considering a single-valley effective mass equation,

$$\left[-\frac{\nabla_x^2}{2m_x}-\frac{\nabla_y^2}{2m_y}-\frac{\nabla_z^2}{2m_z}-\frac{e^2}{4\pi\varepsilon_{Si}r}\right]F(\mathbf{r})=EF(\mathbf{r}). \tag{66}$$

We consider the specific case of a valley in which the x and y masses are transverse and the z mass is longitudinal,

$$\left[-\frac{\nabla_x^2}{2m_\perp}-\frac{\nabla_y^2}{2m_\perp}-\frac{\nabla_z^2}{2m_\parallel}-\frac{e^2}{4\pi\varepsilon_{Si}r}\right]F(\mathbf{r})=EF(\mathbf{r}). \tag{67}$$

The parameter, $\gamma=\frac{m_\parallel}{m_\perp-m_\parallel}$, is introduced such that this can be rewritten as,

$$\left[-\frac{\nabla^2}{2m_\perp}-\frac{\nabla_z^2}{2\gamma m_\perp}-\frac{e^2}{4\pi\varepsilon_{Si}r}\right]F(\mathbf{r})=EF(\mathbf{r}), \tag{68}$$

which is evidently a hydrogenic Hamiltonian with a correction to its kinetic energy. The kinetic energy correction breaks the separability of the PDE in spherical coordinates. In what follows, we construct a separable basis of hydrogenic orbitals and use it to solve Eq. 68.

If we ignore the kinetic energy correction that breaks spherical symmetry, we are left with a separable PDE,

$$\left[-\frac{\nabla^2}{2m_\perp}-\frac{e^2}{4\pi\varepsilon_{Si}r}\right]F(\mathbf{r})=EF(\mathbf{r}). \tag{69}$$

We know the complete spectrum of hydrogenic solutions. The bound states are given as,

$$f_{nlm}(\mathbf{r})=R_{nl}(r)Y_{lm}(\theta,\phi), \tag{70}$$

where n, l, and m are the radial, angular, and magnetic quantum numbers, $Y_{lm}(\theta,\phi)$ is a spherical harmonic, and $R_{nl}(r)$ is given as,

$$\sqrt{\left(\frac{2}{na_\perp}\right)^3\frac{(n-l-1)!}{2n[(n+l)!]}}e^{-r/na_\perp}\left(\frac{2r}{na_\perp}\right)^l L_{n-l-1}^{2l+1}\left(\frac{2r}{na_\perp}\right), \tag{71}$$

where $L_{n-l-1}^{2l+1}(u)$ is an associated Laguerre polynomial. The effective Bohr radius,

$$a_\perp=\frac{4\pi\varepsilon_{Si}\hbar^2}{m_\perp e^2} \tag{72}$$

is for an electron with an isotropic effective mass equivalent to $m_\perp$ in a medium in which the strength of the static Coulomb interaction is renormalized by the dielectric constant of silicon. The energies of these eigenfunctions are determined entirely by the radial quantum number, n,

$$e_n=-\left(\frac{m_\perp e^4}{32\pi^2\varepsilon_{Si}^2\hbar^2}\right)\frac{1}{n^2} \tag{73}$$

.

We use these bound state solutions as a basis for a solution to the fully anisotropic problem, 68,

$$F(\mathbf{r}) = \sum_{nlm} c_{nlm} f_{nlm}(\mathbf{r}). \tag{74}$$

Inserting this into Eq. 68, we are left with

$$\sum_{nlm} c_{nlm} \left(e_n - \frac{\nabla_z^2}{2\gamma m_\perp} \right) f_{nlm}(\mathbf{r}) = E \sum_{nlm} c_{nlm} f_{nlm}(\mathbf{r}), \tag{75}$$

which can be projected onto a particular basis function, $f_{n'l'm'}(\mathbf{r})$,

$$e_n \delta_{nlm}^{n'l'm'} + \Delta_{nlm}^{n'l'm'} = E \delta_{nlm}^{n'l'm'}. \tag{76}$$

Here, $\delta_{nlm}^{n'l'm'}$ is a Kronecker delta symbol that evaluates to zero unless the integer strings in the subscript and superscript are identical. Eq. 76 defines an eigenvalue problem in terms of the bare orbital energies and matrix elements of the anisotropic correction to the kinetic energy. These matrix elements are given as

$$\Delta_{nlm}^{n'l'm'} = -\int_0^\infty dr \int_0^\pi d\theta \int_0^{2\pi} d\phi \; r^2 \sin(\theta) R_{n'l'}^*(r) Y_{l'm'}^*(\theta,\phi) \frac{\nabla_z^2}{2\gamma m_\perp} R_{nl}(r) Y_{lm}(\theta,\phi). \tag{77}$$

In the following subsection we evaluate this integral.

A.1. Matrix elements for the anisotropic correction to the kinetic energy

Integration by parts can be applied to Eq. 77 and the matrix elements are then rendered as,

$$\Delta_{nlm}^{n'l'm'} = \frac{1}{2\gamma m_\perp} \int_0^\infty dr \int_0^\pi d\theta \int_0^{2\pi} d\phi \; r^2 \sin(\theta) \frac{\partial}{\partial z} \Big(R_{n'l'}^*(r) Y_{l'm'}^*(\theta,\phi) \Big) \frac{\partial}{\partial z} \Big(R_{nl}(r) Y_{lm}(\theta,\phi) \Big). \tag{78}$$

Because the z derivative does not act on the ϕ coordinate, we can evaluate the ϕ integral directly,

$$\Delta_{nlm}^{n'l'm'} = \delta_m^{m'} \mathcal{N}_{lm}^{l'm} \int_0^\infty dr \int_0^\pi d\theta \; r^2 \sin(\theta) \frac{\partial}{\partial z} \Big(R_{n'l'}(r) P_{l'}^{m'}(\cos(\theta)) \Big) \frac{\partial}{\partial z} \Big(R_{nl}(r) P_l^m(\cos(\theta)) \Big), \tag{79}$$

where the constant prefactor $\mathcal{N}_{lm}^{l'm}$ is

$$\mathcal{N}_{lm}^{l'm} = \frac{1}{2\gamma m_\perp} \sqrt{(2l+1)(2l'+1) \frac{(l-m)!(l'-m)!}{(l+m)!(l'+m)!}}, \tag{80}$$

$P_l^m(u)$ is an associated Legendre polynomial, and we have made use of the fact that $R_{nl}(r)$ is real-valued. Eq. 79 can then be decomposed into a sum of 4 terms,

$$\Delta_{nlm}^{n'l'm'} = \delta_m^{m'} \mathcal{N}_{lm}^{l'm} \left(\mathcal{A}_{nlm}^{n'l'm} + \mathcal{B}_{nlm}^{n'l'm} + \mathcal{C}_{nlm}^{n'l'm} + \mathcal{D}_{nlm}^{n'l'm} \right), \text{ where} \tag{81}$$

$$\mathcal{A}_{nlm}^{n'l'm} = \left(\int_0^\infty dr\, r^2 \frac{\partial R_{n'l'}(r)}{\partial r} \frac{\partial R_{nl}(r)}{\partial r} \right) \left(\int_{-1}^1 du\, u^2 P_{l'}^m(u) P_l^m(u) \right) = A_{nl}^{n'l'} a_{lm}^{l'm}, \tag{82a}$$

$$\mathcal{B}_{nlm}^{n'l'm} = \left(\int_0^\infty dr\, r \frac{\partial R_{n'l'}(r)}{\partial r} R_{nl}(r) \right) \left(\int_{-1}^1 du\, u(u^2-1) P_{l'}^m(u) \frac{\partial P_l^m(u)}{\partial u} \right) = B_{nl}^{n'l'} b_{lm}^{l'm}, \tag{82b}$$

$$\mathcal{C}_{nlm}^{n'l'm} = \left(\int_0^\infty dr\, r \frac{\partial R_{nl}(r)}{\partial r} R_{n'l'}(r) \right) \left(\int_{-1}^1 du\, u(u^2-1) P_l^m(u) \frac{\partial P_{l'}^m(u)}{\partial u} \right) = C_{nl}^{n'l'} c_{lm}^{l'm}, \text{ and} \tag{82c}$$

$$\mathcal{D}_{nlm}^{n'l'm} = \left(\int_0^\infty dr\, R_{n'l'}(r) R_{nl}(r) \right) \left(\int_{-1}^1 du\, (u^2-1)^2 \frac{\partial P_{l'}^m(u))}{\partial u} \frac{\partial P_l^m(u)}{\partial u} \right) = D_{nl}^{n'l'} d_{lm}^{l'm}. \tag{82d}$$

Here we have applied the usual transformation from an integral over $\theta \in [0, \pi]$ to an integral over $u = \cos(\theta) \in [-1, 1]$. Next, we will evaluate the integrals over associated Legendre polynomials to establish selection rules on l and then evaluate the remaining integrals over the radial orbitals.

A.2. Integrals involving associated Legendre polynomials:

To evaluate the integrals over u, we will need three identities. The first is the orthogonality identity,

$$\int_{-1}^1 du\, P_l^m(u) P_{l'}^m(u) = \frac{2}{2l+1} \frac{(l+m)!}{(l-m)!} \delta_l^{l'}. \tag{83}$$

The second is a recurrence relation involving products of the argument and associated Legendre polynomials,

$$u P_l^m(u) = \frac{1}{2l+1} \left[(l-m+1) P_{l+1}^m(u) + (l+m) P_{l-1}^m(u) \right]. \tag{84}$$

The third is an expression for the derivative of an associated Legendre polynomial,

$$(u^2-1) \frac{\partial P_l^m(u)}{\partial u} = l u P_l^m(u) - (l+m) P_{l-1}^m(u). \tag{85}$$

Henceforth, we will suppress the arguments of the associated Legendre polynomials for brevity.

Using Eq. 84, $a_{lm}^{l'm}$ can be written as,

$$a_{lm}^{l'm} = \frac{1}{(2l+1)(2l'+1)} \int_{-1}^1 du \, \left[(l-m+1) P_{l+1}^m + (l+m) P_{l-1}^m \right] \left[(l'-m+1) P_{l'+1}^m + (l'+m) P_{l'-1}^m \right]. \tag{86}$$

Applying the orthogonality identity to this expression, it becomes evident that there are three distinct cases in which this integral is non-zero, $l' = l$ and $l' = l \pm 2$.

$$a_{lm}^{l'm} = \frac{2}{(2l+1)(2l'+1)} \begin{cases} \frac{(l-m+1)(l'-m+1)(l+m+1)!}{(2l+3)(l-m+1)!} + \frac{(l+m)(l'+m)(l+m-1)!}{(2l-1)(l-m-1)!} & \text{when } l' = l, \\ \frac{(l-m+1)(l'+m)(l+m+1)!}{(2l+3)(l-m+1)!} & \text{when } l' = l+2, \\ \frac{(l+m)(l'-m+1)(l+m-1)!}{(2l-1)(l-m-1)!} & \text{when } l' = l-2, \\ 0 & \text{otherwise.} \end{cases} \tag{87}$$

A similar selection rule on l and l' will be evident for the remaining integrals, which renders $\Delta_{nlm}^{n'l'm'}$ sparse.

Using Eq. 84 and Eq. 85, $b_{lm}^{l'm}$ can be written as,

$$b_{lm}^{l'm} = \frac{1}{2l'+1} \int_{-1}^{1} du \left[\frac{l}{2l+1} \{(l-m+1)P_{l+1}^m + (l+m)P_{l-1}^m\} - (l+m)P_{l-1}^m \right] \left[(l'-m+1)P_{l'+1}^m + (l'+m)P_{l'-1}^m \right]. \tag{88}$$

We can again apply the orthogonality identity to evaluate this expression,

$$b_{lm}^{l'm} = \frac{2}{2l'+1} \begin{cases} \frac{l(l-m+1)(l'-m+1)(l+m+1)!}{(2l+1)(2l+3)(l-m+1)!} + \frac{l(l+m)(l'+m)(l+m-1)!}{(2l+1)(2l-1)(l-m-1)!} - \frac{(l+m)(l'+m)(l+m-1)!}{(2l-1)(l-m-1)!} & \text{when } l' = l, \\ \frac{l(l-m+1)(l'+m)(l+m+1)!}{(2l+1)(2l+3)(l-m+1)!} & \text{when } l' = l+2, \\ \frac{l(l+m)(l'-m+1)(l+m-1)!}{(2l+1)(2l-1)(l-m-1)!} - \frac{(l+m)(l'-m+1)(l+m-1)!}{(2l-1)(l-m-1)!} & \text{when } l' = l-2, \\ 0 & \text{otherwise.} \end{cases} \tag{89}$$

This result can be recycled if we notice that $b_{lm}^{l'm}$ and $c_{lm}^{l'm}$ are trivially related by a relabeling of indices,

$$c_{lm}^{l'm} = b_{l'm}^{lm}. \tag{90}$$

Finally, we rewrite $d_{lm}^{l'm}$ as

$$d_{lm}^{l'm} = \int_{-1}^{1} du \ \left[luP_l^m - (l+m)P_{l-1}^m \right] \left[l'uP_{l'}^m - (l'+m)P_{l'-1}^m \right]. \tag{91}$$

It is convenient to expand the product of sums in the integrand and to commute summation and integration, leaving

$$\begin{aligned} d_{lm}^{l'm} =& (l+m)(l'+m) \int_{-1}^{1} du \ P_{l-1}^m P_{l'-1}^m - l(l'+m) \int_{-1}^{1} du \ uP_l^m P_{l'-1}^m \\ & - l'(l+m) \int_{-1}^{1} du \ uP_{l-1}^m P_{l'}^m + ll' \int_{-1}^{1} du \ u^2 P_l^m P_{l'}^m \end{aligned} \tag{92}$$

The last term is evidently proportional to $a_{lm}^{l'm}$ and the remaining integrals can be evaluated using the same identities as before, leading to

$$d_{lm}^{l'm} = ll' a_{lm}^{l'm} + \begin{cases} \frac{2(l+m)(l'+m)(l+m-1)!}{(2l-1)(l-m-1)!} - \frac{2l(l'+m)(l+m)(l+m-1)!}{(2l+1)(2l-1)(l-m-1)!} - \frac{2l'(l+m)(l-m)(l+m)!}{(2l-1)(2l+1)(l-m)!} & \text{when } l' = l, \\ -\frac{2l(l'+m)(l-m+1)(l+m+1)!}{(2l+1)(2l+3)(l-m+1)!} & \text{when } l' = l+2, \\ -\frac{2l'(l+m)(l+m-1)(l+m-2)!}{(2l-1)(2l-3)(l-m-2)!} & \text{when } l' = l-2, \\ 0 & \text{otherwise.} \end{cases} \tag{93}$$

A.3. Integrals involving associated Laguerre polynomials:

First, it is useful to restate the definition of the radial wave function to introduce notational shorthands,

$$R_{nl}(r) = \sqrt{\left(\frac{2}{na_\perp}\right)^3 \frac{(n-l-1)!}{2n[(n+l)!]}} e^{-r/na_\perp} \left(\frac{2r}{na_\perp}\right)^l L_{n-l-1}^{2l+1}\left(\frac{2r}{na_\perp}\right) = \mathcal{R}_{nl} e^{-u/2n} \left(\frac{u}{n}\right)^l L_{n-l-1}^{2l+1}\left(\frac{u}{n}\right), \tag{94}$$

where $u = 2r/a_\perp$. This function's derivative is then conveniently rendered as,

$$\frac{\partial R_{nl}(r)}{\partial r} = \mathcal{R}_{nl} e^{-u/2n} \frac{1}{n^2 a_\perp} \left(\frac{u}{n}\right)^{l-1} \left[(2nl-u) L_{n-l-1}^{2l+1}\left(\frac{u}{n}\right) - 2u L_{n-l-2}^{2l+2}\left(\frac{u}{n}\right)\right]. \tag{95}$$

Inserting this expression into the radial integrals in Eq. 79, we see that we will need to evaluate integrals of the form,

$$I_{pq}^{rs}[\alpha,\beta] = \int_0^\infty du\, e^{-\alpha u/2} u^{\beta-1} L_p^r(\alpha_1 u) L_q^s(\alpha_2 u), \text{ where } \alpha = \alpha_1 + \alpha_2. \tag{96}$$

The 1 subtracted from $u^{\beta-1}$ was so chosen as to simplify the expressions that we will derive below. To begin evaluating this integral, we recall that the associated Laguerre polynomials can be expressed in terms of generalized hypergeometric functions,

$$L_p^r(\alpha_1 u) = \frac{(r+1)_p}{p!} {}_1F_1(-p; r+1; \alpha_1 u). \tag{97}$$

We recall the definitions of the Pochhammer symbol and the generalized hypergeometric function as,

$$(a)_p = \frac{\Gamma(a+p)}{\Gamma(a)},\ (a)_0 = 1,\ (-a)_p = (-a)(-a+1)\ldots(-a+p-1) \tag{98a}$$

$${}_mF_n[a_1\ldots a_m; b_1\ldots b_n; z] = \sum_{l=0}^\infty \frac{(a_1)_l \ldots (a_m)_l}{(b_1)_l \ldots (b_n)_l} \frac{z^l}{l!} \tag{98b}$$

For the Pochhammer symbol, we have presented both a definition in terms of gamma functions for the sake of certain identities, and as a rising factorial. This allows us to easily see that

$(-a)_p = 0$ for $p > a$, which renders certain infinite sums as finite. For example, the negative argument in Eq. 97 terminates the otherwise infinite hypergeometric series to generate a polynomial of finite order. Plugging in the definition of the associated Laguerre polynomials in terms of hypergeometric functions and expanding that definition we can write Eq. 96 as,

$$I^{rs}_{pq}[\alpha,\beta] = \frac{(r+1)_p(s+1)_q}{r!s!}\sum_{m,n=0}^{p,q}\frac{(-p)_m(-q)_n}{m!n!(r+1)_m(s+1)_n}\alpha_1^m\alpha_2^n\int_0^\infty du\, e^{-\alpha u/2}u^{\beta+m+n-1}. \tag{99}$$

The remaining integral is trivial to evaluate,

$$I^{rs}_{pq}[\alpha,\beta] = \left(\frac{2}{\alpha}\right)^\beta\frac{(r+1)_p(s+1)_q}{r!s!}\sum_{m,n=0}^{p,q}\frac{(-p)_m(-q)_n\Gamma(m+n+\beta)}{m!n!(r+1)_m(s+1)_n}\left(\frac{2\alpha_1}{\alpha}\right)^m\left(\frac{2\alpha_2}{\alpha}\right)^n. \tag{100}$$

We can rewrite this in terms of Appell's F_2 function by noticing that $\Gamma(m+n+\beta) = \Gamma(\beta)(\beta)_{m+n}$,

$$I^{rs}_{pq}[\alpha,\beta] = \left(\frac{2}{\alpha}\right)^\beta\frac{(r+1)_p(s+1)_q\Gamma(\beta)}{r!s!}\sum_{m,n=0}^{p,q}\frac{(-p)_m(-q)_n(\beta)_{m+n}}{m!n!(r+1)_m(s+1)_n}\left(\frac{2\alpha_1}{\alpha}\right)^m\left(\frac{2\alpha_2}{\alpha}\right)^n,$$

$$I^{rs}_{pq}[\alpha,\beta] = \left(\frac{2}{\alpha}\right)^\beta\frac{(r+1)_p(s+1)_q\Gamma(\beta)}{r!s!}F_2\left[\beta;-p,-q;r+1,s+1;\left(\frac{2\alpha_1}{\alpha}\right),\left(\frac{2\alpha_2}{\alpha}\right)\right]. \tag{101}$$

Here F_2 is a bivariate generalization of the hypergeometric function. Because the second two arguments are negative integers, this is simply a bivariate polynomial in the last two arguments, rather than an infinite series. In point of fact, the power series definition of F_2 is only guaranteed to converge when the L_1-norm of the last two arguments is less than one. We will proceed assuming that this is something for which we can code up a stable evaluation routine without further reduction for the specific instances relevant to our integrals. Nevertheless, there are likely tricks that we can do to reduce this to a single hypergeometric function (${}_3F_2$) if necessary.

Next, we render the specific integrals in terms of $I^{rs}_{pq}[\alpha,\beta]$. We begin with $D^{n'l'}_{nl}$ because it is the simplest,

$$D^{n'l'}_{nl} = \int_0^\infty dr\, R_{n'l'}(r)R_{nl}(r) = \mathcal{R}_{n'l'}\mathcal{R}_{nl}\frac{a_\perp}{2n^{l+l'}}\int_0^\infty du e^{-(1/n'+1/n)u/2}u^{l+l'}L^{2l'+1}_{n'-l'-1}\left(\frac{u}{n'}\right)L^{2l+1}_{n-l-1}\left(\frac{u}{n}\right)$$

$$D^{n'l'}_{nl} = \mathcal{R}_{n'l'}\mathcal{R}_{nl}\frac{a_\perp}{2n^l n'^{l'}}I^{2l+1,2l'+1}_{n-l-1,n'-l'-1}\left[\frac{1}{n}+\frac{1}{n'},l+l'+1\right]. \tag{102}$$

From numerical experimentation in Mathematica, the only selection rule appears to be that this integral is zero if $n = n'$ and $l \neq l'$.

There are three integrals comprising $C_{nl}^{n'l'}$ and $B_{nl}^{n'l'}$, which are themselves related as $B_{nl}^{n'l'} = C_{n'l'}^{nl}$.

$$\begin{aligned}
C_{nl}^{n'l'} &= \int_0^\infty dr\, r \frac{\partial R_{nl}}{\partial r} R_{n'l'}(r) \\
&= \mathcal{R}_{nl}\mathcal{R}_{n'l'} \frac{a_\perp}{4n^{l+1}n'^{l'}} \int_0^\infty du\, e^{-(1/n+1/n')u/2} u^{l+l'} \left[(2nl-u)\, L_{n-l-1}^{2l+1}\left(\frac{u}{n}\right) - 2uL_{n-l-2}^{2l+2}\left(\frac{u}{n}\right)\right] L_{n'-l'-1}^{2l'+1}\left(\frac{u}{n'}\right) \\
&= \mathcal{R}_{nl}\mathcal{R}_{n'l'} \frac{a_\perp}{4n^{l+1}n'^{l'}} \left(2nl\, I_{n-l-1,n'-l'-1}^{2l+1,2l'+1}\left[\frac{1}{n}+\frac{1}{n'}, l+l'+1\right] - I_{n-l-1,n'-l'-1}^{2l+1,2l'+1}\left[\frac{1}{n}+\frac{1}{n'}, l+l'+2\right] \ldots \right. \\
&\left. \ldots - 2\, I_{n-l-2,n'-l'-1}^{2l+2,2l'+1}\left[\frac{1}{n}+\frac{1}{n'}, l+l'+2\right]\right). \qquad (103)
\end{aligned}$$

Numerical experimentation in Mathematica doesn't appear to indicate that there are any selection rules to make use of for these integrals.

Finally, we consider $A_{nl}^{n'l'}$ which consists of nine integrals. Noticing that the first argument of I is always $1/n+1/n'$, we will suppress it henceforth.

$$\begin{aligned}
A_{nl}^{n'l'} &= \int_0^\infty dr\, r^2 \frac{\partial R_{nl}}{\partial r}\frac{\partial R_{n'l'}}{\partial r} \\
&= \mathcal{R}_{nl}\mathcal{R}_{n'l'} \frac{a_\perp^2}{8n^{l+1}n'^{l'+1}} \int_0^\infty du\, e^{-(1/n+1/n')u/2} u^{l+l'} \left[(2nl-u)\, L_{n-l-1}^{2l+1}\left(\frac{u}{n}\right) - 2uL_{n-l-2}^{2l+2}\left(\frac{u}{n}\right)\right] \ldots \\
&\ldots \times \left[(2n'l'-u)\, L_{n'-l'-1}^{2l'+1}\left(\frac{u}{n'}\right) - 2uL_{n'-l'-2}^{2l'+2}\left(\frac{u}{n'}\right)\right] \\
&= \mathcal{R}_{nl}\mathcal{R}_{n'l'} \frac{a_\perp^2}{8n^{l+1}n'^{l'+1}} \left(4nn'll'\, I_{n-l-1,n'-l'-1}^{2l+1,2l'+1}\left[\cdot, l+l'+1\right] - 2nl\, I_{n-l-1,n'-l'-1}^{2l+1,2l'+1}\left[\cdot, l+l'+2\right] \ldots \right. \\
&\ldots - 4nl\, I_{n-l-1,n'-l'-2}^{2l+1,2l'+2}\left[\cdot, l+l'+2\right] - 2n'l'\, I_{n-l-1,n'-l'-1}^{2l+1,2l'+1}\left[\cdot, l+l'+2\right] + I_{n-l-1,n'-l'-1}^{2l+1,2l'+1}\left[\cdot, l+l'+3\right] \ldots \\
&\ldots + 2\, I_{n-l-1,n'-l'-2}^{2l+1,2l'+2}\left[\cdot, l+l'+3\right] - 4n'l'\, I_{n-l-2,n'-l'-1}^{2l+2,2l'+1}\left[\cdot, l+l'+2\right] + 2\, I_{n-l-2,n'-l'-1}^{2l+2,2l'+1}\left[\cdot, l+l'+3\right] \ldots \\
&\left. \ldots + 4\, I_{n-l-2,n'-l'-2}^{2l+2,2l'+2}\left[\cdot, l+l'+3\right]\right). \qquad (104)
\end{aligned}$$

This is an unwieldy expression, but we can have a computer evaluate it. Yet again, there are no obvious selection rules.

DISTRIBUTION

Hardcopy—Internal

Number of Copies	Name	Org.	Mailstop
1	Andrew Baczewski	01425	1323
1	Dwight Luhman	01879	1304
1	Shashank Misra	05229	0892

Email—Internal (encrypt for OUO)

Name	Org.	Sandia Email Address
Technical Library	01177	libref@sandia.gov

Sandia National Laboratories is a multimission laboratory managed and operated by National Technology & Engineering Solutions of Sandia LLC, a wholly owned subsidiary of Honeywell International Inc., for the U.S. Department of Energy's National Nuclear Security Administration under contract DE-NA0003525.